PREFACE TO THE EDITION

It is with great pleasure that we present this issue of the **International Journal of Pure Science Research Studies (IJPSRS)**, bringing together five scholarly contributions that reflect the diversity and interdisciplinary nature of contemporary scientific research. The articles cover important areas of astronomy, materials science, biological sciences, mathematics, and animal behaviour, demonstrating how scientific inquiry continues to expand our understanding of natural phenomena and emerging scientific challenges.

The issue opens with an exploration of how polarimetry helps assess the surface properties of asteroids and the Moon. The article examines the polarization of scattered sunlight, focusing on phase-polarization curves and the influence of particle size and composition. It also discusses methods for estimating grain sizes and the relationship between polarimetric parameters and geometric albedo, highlighting the importance of these measurements in understanding planetary surface characteristics.

The field of materials science and environmental technology is represented by a review of metal-organic frameworks for carbon dioxide capture. The article examines their structural design, adsorption mechanisms, and performance in separating carbon dioxide from flue gas and atmospheric air. Particular attention is given to working capacity, selectivity, regeneration energy, and material stability, highlighting their potential for developing efficient and practical carbon capture technologies.

The biological sciences are represented by an examination of amphibian declines associated with fungal diseases, particularly chytridiomycosis. The article discusses the pathogens responsible for widespread amphibian population losses, their effects on essential physiological processes, and the factors influencing disease outcomes. It also highlights the role of international amphibian trade in pathogen spread and examines conservation measures such as biosecurity, trade regulation, and captive assurance programmes.

A significant mathematical contribution to this issue examines the total stopping times associated with the Collatz map. Through computational analysis of integers up to 10^7, the study evaluates the random-walk model and its predictions concerning the mean, variance, and distribution of stopping times. The findings show considerable agreement with theoretical predictions while identifying certain deviations, demonstrating the value of computational methods in investigating unresolved mathematical problems.

Completing this issue is an exploration of magnetic orientation and navigation in migratory animals. The article examines how species such as birds, sea turtles, salmon, and butterflies use the Earth's magnetic field for directional guidance and navigation. It discusses the proposed radical-pair mechanism involving cryptochrome proteins and the role of biogenic magnetite, while highlighting the continuing scientific efforts to identify the precise sensory mechanisms involved.

Taken together, the contributions in this issue illustrate the diversity of contemporary pure science and the connections between theoretical understanding, experimental investigation, and computational research. From planetary surface studies and carbon capture technologies to biodiversity conservation, mathematical modelling, and animal navigation, these articles demonstrate the continuing importance of scientific inquiry in advancing knowledge across disciplines.

We hope that this issue of IJPSRS will provide researchers, academicians, students, and scientific professionals with valuable insights and encourage further investigation, interdisciplinary dialogue, and scholarly collaboration.

We sincerely thank all the authors, reviewers, and editorial contributors whose efforts have made this issue possible. We look forward to continuing our commitment to disseminating rigorous and meaningful research through the International Journal of Pure Science Research Studies.

Dr. Sandhya E
Chief editor

CONTENTS

SL. NO.	TITLE	AUTHOR	PAGE NO.
1	Polarimetry as a tool to assess the surface properties of asteroids and the Moon	Zokapsang Lungtau	1-7
2	Metal-Organic Frameworks for Carbon Dioxide Capture: Design Principles and Performance	Teena Joseph	8-12
3	Amphibian Declines and Chytridiomycosis: Pathogen Biology, Impacts and Conservation Responses	Anjaly Jose	13-17
4	Total Stopping Times of the Collatz Map up to 10^7: A Computational Test of the Random-Walk Model	Lejo J Manavalan	18-22
5	Magnetoreception and Navigation in Migratory Animals: Mechanisms and Evidence	Jeeva Chacko	23-27

INTERNATIONAL JOURNAL OF PURE SCIENCE RESEARCH STUDIES (IJPSRS)
(Open Access, Double-Blind Peer Reviewed Journal)
ISSN Online: 3139-8995



Polarimetry as a tool to assess the surface properties of asteroids and the Moon

Zokapsang Lungtau

Assistant Professor, Department of Physics, Dhakuakhana college (Autonomous), Assam, India

Article Information

Received: 25th September 2026
Received in revised form: 10th October 2026
Accepted: 27th October 2026
Available online: 3rd November 2026

Volume: 2
Issue: 4
DOI: https://doi.org/10.63090/IJPSRS/3139.8995.0023

Abstract

The polarization of sunlight scattered by atmosphereless Solar System bodies depends on the surface properties of the scattering medium. The surface properties of the scattering medium can be inferred from the study of polarization of the scattered sunlight. The polarization is generally measured as a function of phase angle. This paper reviews the exploration of phase-polarization curves to characterize the surfaces of asteroids and the Moon. The effects of particle size and composition on the phase-polarization curve are also discussed. Methods for estimating characteristic grain sizes from polarization measurements, and empirical relationships between polarimetric parameters and the geometric albedo are also discussed. However, these empirical relationships need proper calibration. The albedo values of asteroids, obtained from different polarimetric parameters, show a remarkable consistency, except for Barbarian asteroids. The locations of most of the asteroids in the $P_{\min} - \alpha_{\text{inv}}$ plane were found in a region between those occupied by bare rocks ($\alpha_{\text{inv}} < 18^0$) and by lunar fines ($18^0 \leq \alpha_{\text{inv}} \leq 25^0$), indicating that asteroid surfaces are covered by a regolith that is coarser than lunar surface, but finer than bare rocks. Lunar surface particle sizes were estimated to be about 50–100 mm.

Keywords: Phase-Polarization, Diagnostic Tools, Albedo, Asteroids, Moon

1. INTRODUCTION

Polarization is a fundamental property of electromagnetic radiation. The polarization state is related to the time variations of the electric field in a plane perpendicular to the direction of propagation. If the electric field varies randomly in time, then the wave is said to be unpolarized. On the contrary, if it varies in a preferable direction, it is said to be polarized.

An individual electromagnetic wave is essentially polarized. However, all natural radiations are a superposition of very large number of individual electromagnetic waves.[1] Therefore, for most physical systems, all orientations of the electric field vectors from the individual emitters are equally probable. Due to this reason, natural light is therefore sometimes referred to as "unpolarized" light. Polarization can occur whenever the internal geometry of the source of radiation or the interacting medium prefers a certain orientation of electric field vectors. In those cases, the radiation becomes partially polarized with a degree of polarization (DOP) given as

$$\text{DOP} = \frac{I_P}{I} \in [0,1]$$

where I denotes the total intensity of the radiation, and I_P denotes the intensity of polarized radiation. For fully polarized light DOP is 1, for unpolarized light it is 0, and for partially polarized light it lies between 0 and 1. The polarization state of light is determined by the Stokes parameters.[2]

2. PHASE-POLARIZATION CURVE

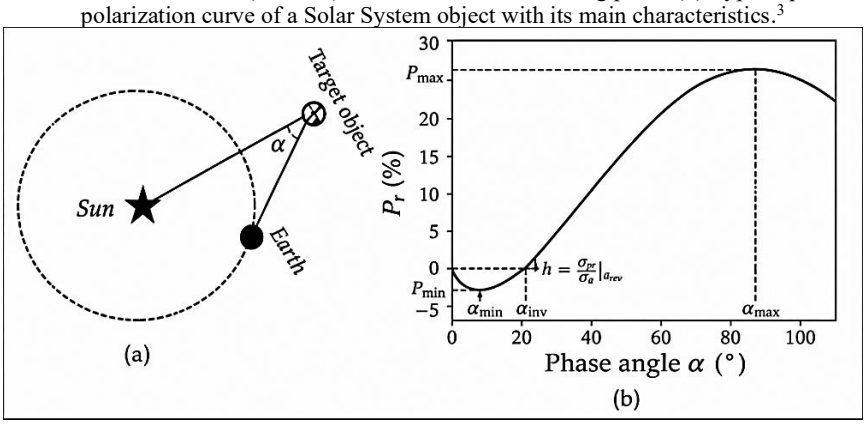
Observations of astronomical or solar system bodies rely on measurement of intensity of light coming from the body. However, light carries far more information than intensity alone can provide. Polarization of light has been exploited in polarimetric techniques to study the surface properties of astronomical objects. Planets, asteroids, comets, moons, and others solar system bodies scatter sunlight that is incident upon them. The scattered light from these objects is generally polarized. The total fraction of linear polarization of the scattered light received by the observer is given as [3]

$$P_r(\lambda) = \frac{I_\perp(\lambda) - I_\parallel(\lambda)}{I_\perp(\lambda) + I_\parallel(\lambda)} \quad (1)$$

where $I_\perp(\lambda)$ and $I_\parallel(\lambda)$ are the intensities at wavelength λ, measured through a linear polarizer perpendicular or parallel to the scattering plane (i.e., the plane that contains both the direction of the incident light and the direction of the scattered light), respectively. The sign of $P_r(\lambda)$ indicates the orientation of the polarization plane; a positive sign indicates that the polarization is perpendicular to the scattering plane, and a negative sign indicates that it is parallel to the scattering plane.

Most of the polarimetric studies are based on observation of $P_r(\lambda)$ as a function of phase angle α (i.e., the angle between the directions to the Sun and to the observer, as seen from the scattering point, see Fig. 1(a)). This is called phase-polarization curve. A typical phase-polarization curve for solar system bodies is shown in Fig. 1(b). The interval of phase angles for which P_r is negative is called the negative polarization branch (NPB). Minimum polarization $P_{\min}$ occurs at phase angle $\alpha_{\min}$ in the NPB. The morphology of the phase-polarization curve is sensitive to the surface structure and composition of the scattering medium. Early observations [4–8] have shown that at visible wavelengths, the sunlight scattered from small bodies of the Solar System is in a state of partial linear polarization, and that the polarization is always either perpendicular or parallel to the scattering plane.

Fig. 1: (a) Illustration of the phase angle α, i.e., the angle between the directions to the Sun and to the observer (on earth), as seen from the scattering point. (b) Typical phase-polarization curve of a Solar System object with its main characteristics.[3]



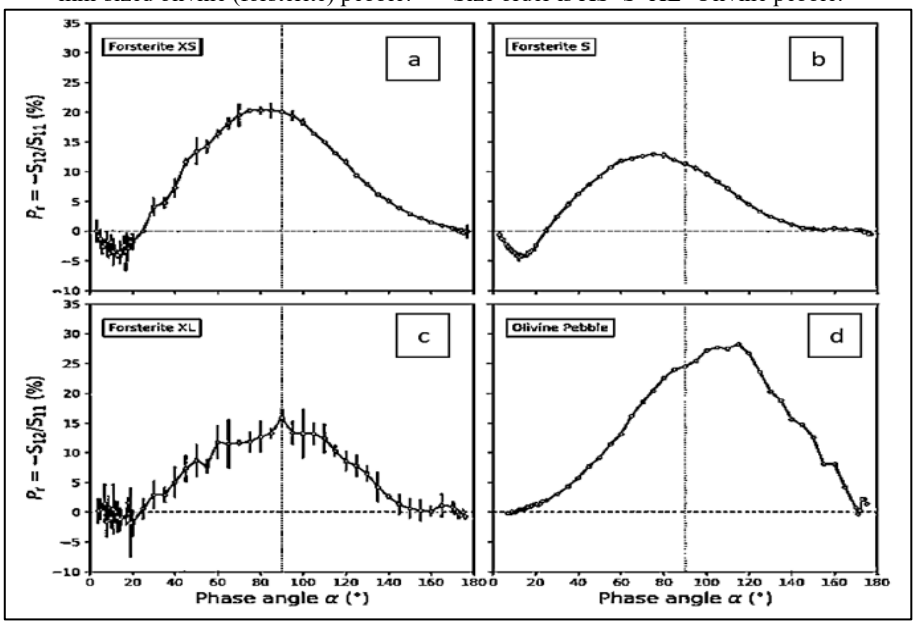
Dust particles on the surfaces of planets, comets, and asteroids consist of irregular refractory materials, spanning over a broad range of composition and morphologies. Further, they are distributed in size from sub-micron region up to tens of microns, or even mm-cm sizes.[3] In addition to offering insights about the composition and history of Solar System planets, these particles have practical implications for space exploration and design of spacecraft and equipment. The analysis of the morphology of the observed phase-polarization curve provides information on the physical characteristics of the scattering dust particles. The phase-polarization curve depends not only on the particle size, but on the ratio of the size to the wavelength, i.e., on the so-called size parameter ($s = 2\pi r/\lambda$), where r denotes the particle radius and λ denotes the wavelength of the incident radiation. Further, the size distribution of cloud of dust particles is typically described by two parameters:[9] (a) the effective radius (r_{eff}) - an area weighted mean radius of the dust size distribution, (b) and the effective variance (v_{eff}) - a measure of the width of the size distribution. From the effective radius value, we can obtain the corresponding effective size parameter ($s_{\text{eff}} = 2\pi r_{\text{eff}}/\lambda$) at the experiment's wavelengths. Whereas, the dust composition is characterized by its complex refractive index as a function of wavelength.

2.1. Size Effects on the Phase-Polarization Curve

Dust particle sizes have significant influences on the phase-polarization curve.[10–14] The phase-polarization curves for magnesium-rich olivine samples [10] of different size parameters are shown in the Fig. 2. For very small particles (sizes smaller than or of the order of the wavelength of the incident light), $P_{\max}$ tends to decrease as the particle size increases into the resonance regime (compare Fig. 2a and 2b). However, the tendency of decreasing values

of $P_{\max}$ with increasing the size parameter is reversed as the size parameter increases into the geometric-optics domain. In the case of $r \gg \lambda$, $P_{\max}$ increases with particle size. Further, as particle size increases into the geometric-optics regime, the position of the maximum value $P_{\max}$ is shifted towards larger phase angles (compare Fig. 2c and 2d). The deepest NPB is observed for particles of size parameter of the order of the wavelength of the incident light. As the dust grain size parameter increases, the NBP becomes shallower and vanishes within the geometric-optics domain. Thus, the maximum value of the polarization and negative polarization branch (NPB) - its magnitude and the inversion angle location, are highly dependent on the size scattering regime.

Fig. 2: Phase-polarization curves for samples forsterite XS, forsterite S, forsterite XL, and mm-sized olivine (forsterite) pebble.[12,14] Size order is XS<S<XL<Olivine pebble.



2.2. Composition Effects on the Phase-Polarization Curve

Dust particles compositions also have significant influences on the phase-polarization curve. Two sets of samples with similar effective size parameters and particle morphology, but significant differences in their refractive indices at the measurement wavelength were prepared.[15,16] The phase-polarization curves are shown in the Fig. 3 and 4. In the case of samples with sizes belonging to the resonance and geometric-optics regimes (Fig. 3(b), 4(a), and 4(b)), $P_{\max}$ is higher for higher absorbing sample. Also, the larger the particle size parameter, the stronger the differences in $P_{\max}$ between low- and high-absorbing samples. There is no significant difference in the maximum of the P_r-curve for the samples belonging to the Rayleigh–resonance transition size regime (Fig. 3(a)). In all the three size scattering regimes, a higher absorption produces deeper negative polarization branch.

Fig. 3: (a) Measured degree of linear polarization curves in percentage as functions of the phase angle for forsterite XS and JSC Mars1 S in the Rayleigh–resonance transition size regime. The imaginary part of the refractive index for the JSC Mars 1 sample is nearly two orders of magnitude higher than the value for the forsterite samples at the measured wavelengths, (b) Measured degree of linear polarization curves in percentage as functions of the phase angle for forsterite S and JSC Mars1 M in the resonance regime. The imaginary part of the refractive index for the JSC Mars 1 sample is nearly two orders of magnitude higher than the value for the forsterite samples at the measured wavelengths.

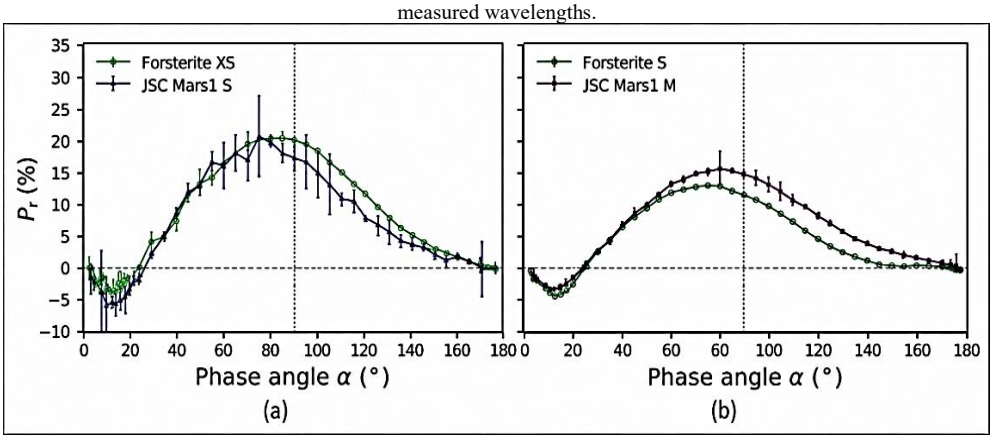
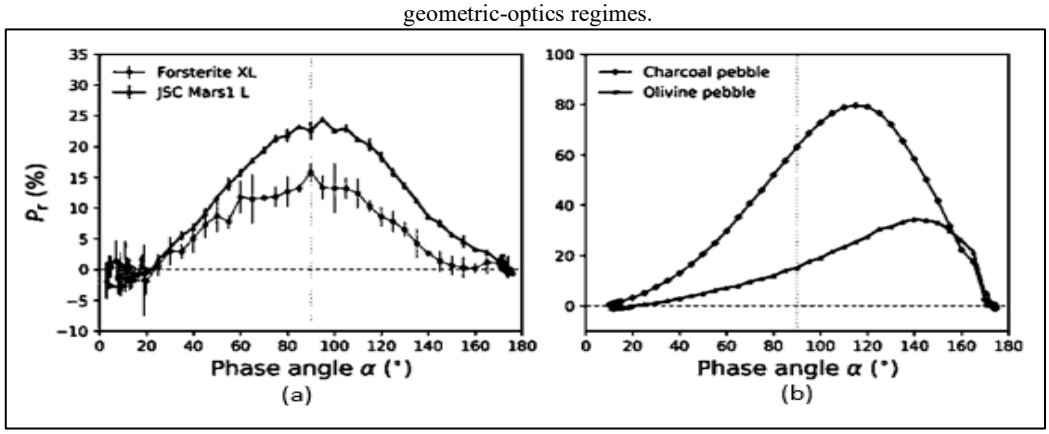


Fig. 4: (a) Measured degree of linear polarization curves in percentage as functions of the phase angle for forsterite XL and JSC Mars1 L in the geometric-optics regimes, (b) Measured degree of linear polarization curves in percentage as functions of the phase angle for Olivine and Charcoal pebbles in the geometric-optics regimes.



3. POLARIMETRIC PARAMETERS AS DIAGNOSTIC TOOLS

The polarization properties of sunlight scattered by atmosphereless solar system bodies have been investigated since a long time, because in principle they can be a source of information about the surface's physical properties of the bodies. However, the interpretation of polarimetric observations of these objects in terms of physical parameters is still not straightforward. The inferences about the surface properties as derived from polarimetric measurements are mostly based on empirical relationships, such as, the relationship between the polarimetric parameters and the albedo, the analysis of similarities and differences in the polarization behaviour.

3.1. Albedo Derived from Polarimetric Parameters

The intuitive idea of surface's inherent brightness or darkness at visible wavelengths is quantified by geometric albedo, which is of fundamental importance to characterize the surface's properties - its composition as well as the macroscopic and microscopic roughness and texture of the surface layer. Though, there are several methods of estimations, an estimate of the geometric albedo can be derived directly from polarimetric measurements without any need of additional information from other sources.[4,6,7] Using the exponential–linear relation, suitable calibrations of several relations between the geometric albedo and the polarimetric parameters can be investigated. The general relationship [17] is described as

$$\log(A_V) = c_1 \log(w) + c_2$$

where A_V is the geometric albedo in V light and w is one of the several possible polarimetric parameters, and c_1 and c_2 are unknown quantities to be determined. One of the suitable relations is, between A_V and the slope h of the polarization-phase curve at inversion angle [3], that is,

$$\log(A_V) = c_1 \log(h) + c_2 \quad (2)$$

Various researchers used different values of c_1 and c_2.[18–20] Alternative relations between albedo and polarization parameters have also been suggested in different literatures.[17,20] However, reliable calibration of these empirical relationships is a major challenge, as these relations were derived from laboratory measurements of meteorites.[6] Using various polarimetric parameters, several attempts have been made to improve the calibration.[17,18,20,21]

3.2. Grain size derived from polarimetric parameters

Using lunar soil samples, Shkuratov & Opanasenko examined the relationship of $P_{\max}$ and the grain size (d), and gave the following equations:[22]

$$d = 0.03 \exp(2.9\, b) \quad (3)$$

and

$$b = \log(10^2\ A_{\alpha=5^0}) + a \log(10\ P_{\max})$$

where d denotes the grain size in μm. $a = 0.795$ at 0.43 μm or 0.845 at 0.65 μm. $A_{\alpha=5^0}$ is the albedo at $\alpha = 5^0$.

The relationship between the parameters $P_{\min}$ and α_{inv}, characterizing the negative polarization branch has also long been considered as diagnostic of the surface texture. Laboratory measurements show that the bare silicate rocks and fine-grained lunar samples occupy two distinct domains in the $P_{\min} - \alpha_{\text{inv}}$ plane.[23]

4. ASTEROIDS AND THE MOON

The maximum attainable value of phase angle, which is orbit-dependent, for main belt asteroids rarely exceeds 30^0. In the case of near-Earth asteroids (NEAs) which can have close approaches with the Earth, much higher values of phase angle are possible, up to more than 100^0 in some circumstances. The availability of a high-quality data set of phase–polarization curves to obtain best-fitting representations using the exponential–linear relation enables us to conduct some updated investigations of the polarimetric characteristics of various classes of asteroids, not limited to just calculating the geometric albedo.

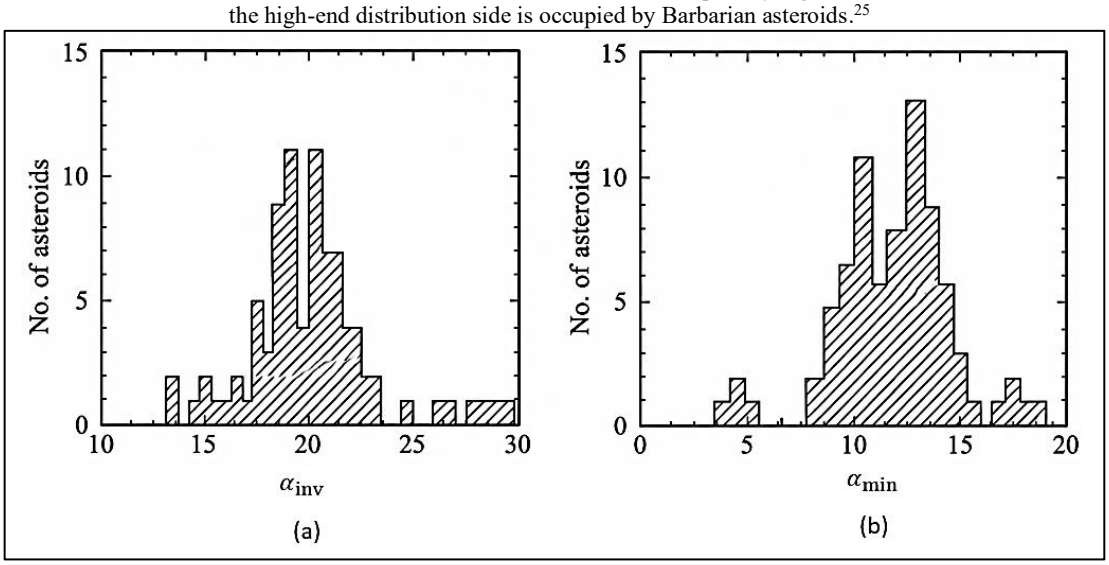
Observations of a particular asteroid, obtained at very different epochs, corresponding to a wide variety of visible and illuminated regions of its surfaces, but at similar phase angles, are fully consistent amongst themselves, except for some cases.[24] This shows that asteroid surfaces are significantly homogeneous, at least in terms of the properties that determine the outcome of light scattering.

The albedo values of asteroids obtained from different polarimetric parameters can be found in the literatures.[17,25] Except for Barbarian asteroids, which have peculiar polarimetric properties, all asteroids albedo values derived using different parameters show a remarkable consistency.

Measured values of parameters describing the phase-polarization curve, particularly the negative branch, were strongly dependent upon the state of fragmentation of the samples.[23] The location of asteroid polarimetric data in the $P_{\min} - \alpha_{\text{inv}}$ plane is considered to be a diagnostic of the average sizes of the particles of the regolith. The locations of most of the asteroids in the $P_{\min} - \alpha_{\text{inv}}$ plane were found in a region between those occupied by bare rocks ($\alpha_{\text{inv}} < 18^0$) and by lunar fines ($18^0 \leq \alpha_{\text{inv}} \leq 25^0$), indicating that asteroid surfaces are covered by a regolith that is coarser than lunar surface, but finer than bare rocks.[3] The asteroids of the same composition class have a tendency to group in the $P_{\min} - \alpha_{\text{inv}}$ plane.[23] This result suggests that a wide range of the inversion angles is most probably related to surface mineralogy rather than to variations of particle size of the regolith. Recently, there have been discovery of unusual objects [25] either having α_{inv} below 18^0 or above 25^0.

The location of Barbarian asteroids in the $P_{\min} - \alpha_{\min}$ plane suggests that their surfaces are covered by extremely fine dust particles.[25] The histograms of α_{inv} and $\alpha_{\min}$ for asteroids are shown in the Fig. 5.

Fig. 5: (a) Histogram of the inversion angle α_{inv} of asteroids. We see that most of the asteroids are centered around 20^0. The low-end distribution side is occupied by F-class asteroids, whereas the high-end distribution side is occupied by Barbarian asteroids,[25] (b) Histogram of the $\alpha_{\min}$ of asteroids. We see that most of the asteroids are centered around 9^0. The low-end distribution side is occupied by high albedo asteroids, whereas the high-end distribution side is occupied by Barbarian asteroids.[25]



The phase-polarization of NEAs can be best described by the formula

$$P_r(\alpha) = A \sin^B(\alpha) \cos^C\left(\frac{\alpha}{2}\right) \sin(\alpha - \alpha_{\text{inv}})$$

where A, B, C, and α_{inv} are parameters to be determined.[26] NEA Icarus shows large values of $\alpha_{\max}, 124^0 \pm 8^0$ in V band and $124^0 \pm 6^0$ in R_C band, which is larger than Moon, Mercury, and other NEAs. Its geometric albedo A_V value is 0.25 ± 0.02 and grain size range is $100 - 130$ μm.[27]

At phase angle $\alpha > 23^0$, the Moon exhibits a positive polarization. The positive branch extends in the direction of larger phase angles at least up to about 165^0.[28] Using the equation (3), the typical range of lunar particle size is found be to 50–100 mm. The highland surface, on an average, is more finely grained. Bright (young) craters have soil with relatively larger particles.

Although the mechanism of negative polarization is still not fully understood, the negative polarization parameters are also closely related to the size of the particles composing the surface and to the degree of its heterogeneity at the scales on the order of the light wavelength.[22,29,30] According to laboratory measurements of finely disperse mixtures of materials with different albedo, of which the lunar regolith is an example, the depth and width of the negative branch significantly increase with the degree of optical heterogeneity of the mixture.[29,30]

5. CONCLUSIONS

The phase-polarization curve contains information about the surface's properties of the scattering medium. In particular, the maximum polarization, minimum polarization, inversion angle, and slope of the polarization curve at inversion, are sensitive to the size, composition, texture, and degree of heterogeneity of surface particles. Particles with sizes comparable to the wavelength of incident light generally produce a pronounced negative polarization branch, whereas this branch becomes weaker as the particle size increases toward the geometric-optics regime. Empirical relationships between geometric albedo and parameters of the phase-polarization curve provide a means of estimating asteroid albedos. Similarly, relationships involving the maximum polarization and albedo can be used to estimate characteristic regolith grain sizes. However, these empirical relationships require a proper calibration. For asteroids, the location of the polarimetric parameters in the $P_{\min} - \alpha_{\text{inv}}$ plane indicates that their surfaces are covered by regolith that is finer than bare rock, but coarser than typical lunar fines. Objects belonging to similar compositional classes tend to show related polarimetric behavior. For the Moon, the depth and width of the negative polarization branch are related not only to particle size but also to the degree of microscopic optical heterogeneity of the surface. Polarimetric measurements complement conventional photometric and spectroscopic observations by providing unique information about the microscopic and macroscopic properties of planetary surfaces.

REFERENCES

1. Trippe S., Polarization and Polarimetry: A Review. 2014 Jan 9. http://arxiv.org/abs/1401.1911. https://doi.org/10.5303/JKAS.2014.47.1.015 .
2. Collett, E., Polarized light. Fundamentals and applications. ui.adsabs.harvard.edu. 1992 [accessed 2026 Sep 4]. https://ui.adsabs.harvard.edu/abs/1992plfa.book.....C/abstract .
3. Bagnulo S et al. Polarimetry of Solar System minor bodies and planets. Astronomy and Astrophysics Review. 2024;32(1). https://doi.org/10.1007/s00159-024-00157-w .
4. Bowell E., Zellner B., Polarization of asteroids and satellites. Planets, Stars, and Nebulae Studied with Photopolarimetry. 1974:381–404.
5. Zellner BH et al., Photometric Properties of the Martian Satellites. Icar. 1974 [accessed 2026 May 29];23(3):437-444. https://ui.adsabs.harvard.edu/abs/1974Icar...23..437Z/abstract . https://doi.org/10.1016/00191035(74)90062-1 .
6. Zellner B et al., Minor planets and related objects. XX. Polarimetric evidence for the albedos and compositions of 94 asteroids. AJ. 1976 [accessed 2026 May 29];81:262–280. https://ui.adsabs.harvard.edu/abs/1976AJ.....81..262Z/abstract . https://doi.org/10.1086/111882 .
7. Zellner B et al., The asteroid albedo scale. I. Laboratory polarimetry of meteorites. LPSC. 1977 [accessed 2026 May 29];1:1091–1110. https://ui.adsabs.harvard.edu/abs/1977LPSC....8.1091Z/abstract .
8. Donati J-F et al., Spectropolarimetric observations of active stars. MNRAS. 1997 [accessed 2026 May 29];291(4):658–682. https://ui.adsabs.harvard.edu/abs/1997MNRAS.291..658D/abstract . https://doi.org/10.1093/MNRAS/291.4.658 .
9. Hansen JE, Travis LD., Light scattering in planetary atmospheres. Space Science Reviews. 1974 [accessed 2026 May 18];16(4):527–610.https://link.springer.com/article/10.1007/BF00168069. https://doi.org/10.1007/BF00168069/METRICS .
10. Muinonen K et al., Light scattering by gaussian random particles: ray optics approximation. Vol 55 1996.
11. Liu J, Yang P, Muinonen K., Dust-aerosol optical modeling with Gaussian spheres: Combined invariant-imbedding T-matrix and geometric-optics approach. Journal of Quantitative Spectroscopy and Radiative Transfer. 2015;161:136–144. https://doi.org/10.1016/j.jqsrt.2015.04.003 .
12. Frattin E et al., Experimental phase function and degree of linear polarization curve of olivine and spinel and the origin of the Barbarian polarization behavior. 2023 Jun 20. http://arxiv.org/abs/2306.11358 .
13. Escobar-Cerezo J et al., Scattering Properties of Large Irregular Cosmic Dust Particles at Visible Wavelengths. The Astrophysical Journal. 2017;838(1):74. https://doi.org/10.3847/1538-4357/aa6303 .
14. Muñoz O et al., Retrieving Dust Grain Sizes from Photopolarimetry: An Experimental Approach. The Astrophysical Journal Supplement Series. 2021;256(1):17. https://doi.org/10.3847/1538-4365/ac0efa .
15. Martikainen J et al., Optical Constants of Martian Dust Analogs at UV–Visible–Near-infrared Wavelengths. The Astrophysical Journal Supplement Series. 2023;268(2):47. https://doi.org/10.3847/1538-4365/acf0be .
16. Muñoz O et al., Experimental Phase Function and Degree of Linear Polarization Curves of Millimeter-sized Cosmic Dust Analogs. The Astrophysical Journal Supplement Series. 2020;247(1):19. https://doi.org/10.3847/1538-4365/ab6851 .
17. Cellino A et al., On the calibration of the relation between geometric albedo and polarimetric properties for the asteroids. Monthly Notices of the Royal Astronomical Society. 2015;451(4):3473–3488. https://doi.org/10.1093/mnras/stv1188 .

18. Lupishko DF, Mohamed RA., A New Calibration of the Polarimetric Albedo Scale of Asteroids. Vol 119 1996.
19. Cellino A et al., On the calibration of the relation between geometric albedo and polarimetric properties for the asteroids. Monthly Notices of the Royal Astronomical Society. 2015 [accessed 2026 May 28];451(4):3473–3488. https://ui.adsabs.harvard.edu/abs/2015MNRAS.451.3473C/abstract . https://doi.org/10.1093/mnras/stv1188 .
20. Masiero JR et al., A revised asteroid polarization-albedo relationship using wise/neowise data. Astrophysical Journal. 2012;749(2). https://doi.org/10.1088/0004-637X/749/2/104.
21. Cellino A et al., A new calibration of the albedo-polarization relation for the asteroids. Journal of Quantitative Spectroscopy and Radiative Transfer. 2012;113(18):2552–2560. https://doi.org/10.1016/j.jqsrt.2012.03.010 .
22. Shkuratov, Yu G, Opanasenko, N V., Polarimetric and Photometric Properties of the Moon: Telescope Observation and Laboratory Simulation 2. The Positive Polarization. Vol 99 1992.
23. Dollfus A, Wolff M, Geake J et al., Photopolarimetry of asteroids. 1989. In: Binzel R, Gehrels T, Matthews M (eds) Asteroids II. University of Arizona Press, Tucson, pp 594–616.
24. Degewij J, Tedesco EF, Zellner B., Albedo and color contrasts on asteroid surfaces. Icarus. 1979 [accessed 2026 Jun 13];40(3):364–374. https://doi.org/10.1016/0019-1035(79)90029-0.
25. Cellino A et al., A polarimetric study of asteroids: Fitting phase-polarization curves. Monthly Notices of the Royal Astronomical Society. 2016;455(2):2091–2100. https://doi.org/10.1093/mnras/stv2445.
26. Goidet-Devel,',' B, Renard' JB, Levasseur-Regourd2 AC., Polarization of asteroids. Synthetic curves and characteristic parameters. Vol 43 1995.
27. Ishiguro M et al., Polarimetric Study of Near-Earth Asteroid (1566) Icarus. The Astronomical Journal. 2017;154(5):180. https://doi.org/10.3847/1538-3881/aa8b1a .
28. Lyot B., Research on polarization of light from planets and... - Google Scholar. 1929 [accessed 2026 May 16]. https://scholar.google.com/scholar?hl=en&as_sdt=0%2C5&q=Research+on+polarization+of+light+from+planets+and+some+terrestrial+substances&btnG=.
29. Shkuratov YG et al., A critical review of theoretical models of negatively polarized light scattered by atmosphereless solar system bodies. Springer, K Muinonen, E Bowell, K Lumme, JI Peltoniemi, MA Kreslavsky, DG Stankevich…Earth, Moon, and Planets, 1994•Springer. 1994 [accessed 2026 Sep 1];65(3):201–246. https://link.springer.com/article/10.1007/BF00579535m . https://doi.org/10.1007/BF00579535 .
30. Shkuratov, Y.G., Negative polarization of sunlight scattered from celestial bodies: interpretation of the wavelength dependence. 1987.

INTERNATIONAL JOURNAL OF PURE SCIENCE RESEARCH STUDIES (IJPSRS)
(Open Access, Double-Blind Peer Reviewed Journal)
ISSN Online: 3139-8995



Metal-Organic Frameworks for Carbon Dioxide Capture: Design Principles and Performance

Teena Joseph

Assistant professor, Department of Chemistry, Nirmalagiri College (Autonomous), Kerala, India

Article Information

Received: 14th July 2026
Received in revised form: 17th August 2026
Accepted: 27th September 2026
Available online: 3rd November 2026

Volume: 2
Issue: 4
DOI: https://doi.org/10.63090/IJPSRS/3139.8995.0024

Abstract

Separating carbon dioxide from flue gas and from air is an adsorption problem with unusually demanding constraints: the target is dilute, the competing components are abundant, water is always present, and the energy spent regenerating the sorbent determines whether the process is worth operating. Metal-organic frameworks address these constraints through structural control that is difficult to achieve in other porous solids, since the metal node and the organic linker can be varied independently and the pore environment adjusted afterwards. This review sets out the three binding mechanisms these materials use, namely physisorption in tailored micropores, coordination at open metal sites, and chemisorption at appended amines, and explains why each produces a characteristic isotherm shape. Performance is then assessed against the criteria that govern practical use, which are working capacity between adsorption and regeneration conditions, selectivity in the presence of nitrogen and water vapour, the heat of adsorption, and stability over repeated cycles. Materials that combine a stepped isotherm with moderate regeneration temperature offer the clearest advantage over aqueous amine scrubbing. Recent work has shifted from record surface areas towards water tolerance, mechanical robustness and inexpensive synthesis, and one framework has now been produced at industrial scale.

Keywords: Metal-Organic Framework, Carbon Capture, Adsorption Isotherm, Cooperative Chemisorption, working capacity

.

1. INTRODUCTION

Post-combustion capture means removing carbon dioxide from a stream that is roughly four fifths nitrogen, contains a few percent oxygen and water vapour, and arrives at atmospheric pressure with the target species at a partial pressure of about 0.15 bar. Aqueous alkanolamine scrubbing has been the reference technology for decades and works reliably, but the solvent must be heated to release the captured gas, and the energy required for that step imposes a large penalty on the efficiency of the plant it serves. [1]Reducing this penalty is the central motivation for research into solid sorbents.

Metal-organic frameworks are crystalline solids in which metal clusters are joined by organic linkers into open, permanently porous networks. Their appeal for separation lies in the degree of control the chemistry offers. Because the framework topology is determined by the geometry of its components, the pore size, the pore shape and the chemical character of the internal surface can each be varied without changing the others, an approach set out under the name reticular synthesis .[2]The first frameworks combining high porosity with permanent structural stability appeared at the end of the 1990s, and surface areas approaching 6000 square metres per gram were

reported within a decade.[3,4,5] Measurements on these early materials also showed that a well-chosen framework could hold more carbon dioxide per unit volume at room temperature than the zeolites then in use.[6]

The early emphasis on surface area proved a poor guide to capture performance. A material with an enormous internal area may adsorb little carbon dioxide at 0.15 bar if its interaction with the molecule is weak, and one that binds very strongly may hold the gas so tightly that recovering it costs more than amine scrubbing. This paper reviews how the field moved from that early emphasis to design criteria that reflect the thermodynamics and the operating conditions of a real separation.

2. HOW FRAMEWORKS BIND CARBON DIOXIDE

Three mechanisms account for almost all of the capture chemistry reported to date, and they produce distinguishable isotherms, shown in Figure 1.[7]

The first is ordinary physisorption in pores whose dimensions are comparable to the molecular diameter. Carbon dioxide has a large quadrupole moment and a higher polarisability than nitrogen, so a narrow pore lined with polar groups favours it even when no specific binding site exists. Uptake rises smoothly with pressure in the manner described by a Langmuir isotherm, and at 0.15 bar the occupancy is modest. Frameworks built with fluorinated pillars, in which hexafluorosilicate anions line a channel of tightly controlled width, illustrate how far selectivity can be pushed by geometry alone.[8,9]

The second mechanism uses coordinatively unsaturated metal centres. When solvent molecules are removed from the metal nodes of certain frameworks, they leave open sites that bind carbon dioxide end-on through the oxygen lone pair. The magnesium form of the dioxidobenzenedicarboxylate series is the standard example: substituting magnesium for other divalent metals raised the uptake at flue-gas partial pressure severalfold, a result that established metal identity as a design variable in its own right.[10] Binding energies at these sites are typically two to three times those of pure physisorption, which shifts most of the adsorption to low pressure and produces the steeply rising isotherm in Figure 1.

The third mechanism is genuine chemisorption. Grafting a diamine onto an open metal site creates a nucleophile positioned within the pore, and carbon dioxide inserts into the metal to nitrogen bond to form an ammonium carbamate. What makes this class distinctive is that insertion at one site facilitates insertion at the next, so the carbamate species propagate in chains along the pore and the isotherm acquires a sharp step rather than a gradual rise.[11] The step position depends on the diamine and on temperature, so it can be tuned to sit just below the partial pressure of the intended feed.[12] Figure 2 shows the pathway. The practical consequence is a large working capacity across a narrow temperature swing, since the step moves with temperature and the material empties almost completely once it has passed.

Fig 1: Characteristic isotherm shapes produced by the three binding mechanisms discussed in Section 2. The dotted line marks the partial pressure of carbon dioxide in typical post-combustion flue gas.

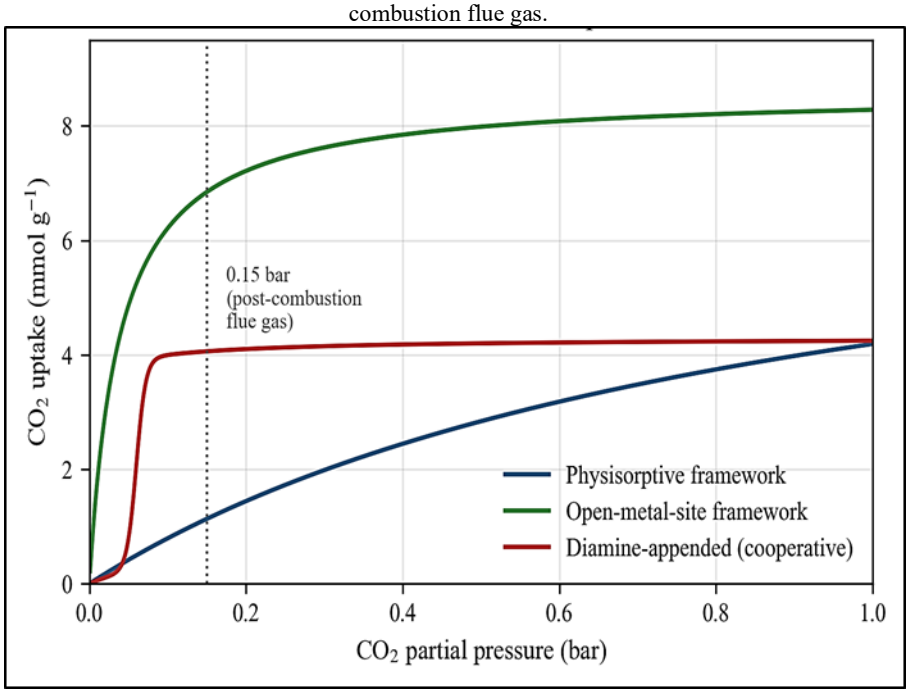
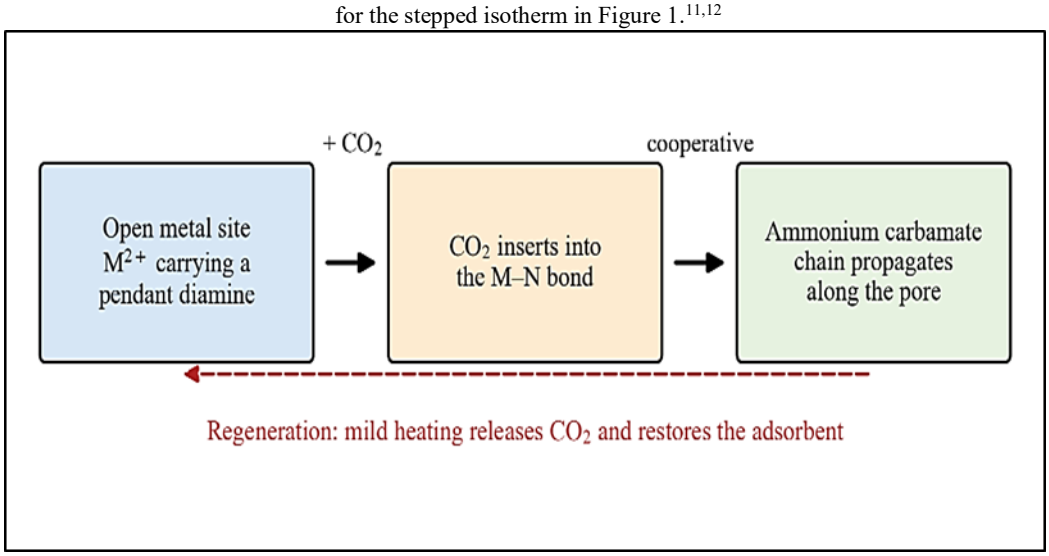


Fig 2: Cooperative insertion of carbon dioxide into a metal-bound diamine, the mechanism responsible for the stepped isotherm in Figure 1.[11,12]



3. CRITERIA THAT DETERMINE PRACTICAL VALUE

Four quantities decide whether an adsorbent is useful, and none of them is the saturation capacity usually quoted in materials papers.

Working capacity is the difference in loading between adsorption and regeneration conditions rather than the loading itself. A material with a steep isotherm may adsorb a great deal at 0.15 bar and still give up very little when heated modestly, because most of its capacity lies below the regeneration point. Stepped isotherms are attractive precisely because the whole step can be traversed by a temperature swing of a few tens of degrees.

Selectivity must be assessed against the whole feed. Ideal adsorbed solution theory applied to single-component isotherms provides a first estimate, but multicomponent measurements are needed where water is present, since water competes for the same polar sites and at open metal centres usually wins [13]. Reports of selectivity obtained under dry conditions overstate performance in service.

The isosteric heat of adsorption sets the energy of regeneration. Values around 30 kilojoules per mole are characteristic of physisorption and cost little to reverse but deliver poor capacity at 0.15 bar; values above 70 correspond to chemisorption and give excellent capacity but require higher temperatures. The optimum for a temperature-swing process lies between these limits, which is the reasoning behind the emphasis on tuning rather than maximising binding strength.[14]

Stability determines whether any of the above survives operation. Many early frameworks hydrolyse in humid gas because the metal to carboxylate bond is susceptible to attack by water. Zirconium-based frameworks resist this through the high charge density of their nodes , and the field now treats water stability as a screening criterion rather than an afterthought .[15,16] Table 1 compares representative materials across these criteria.

Table 1. Representative frameworks studied for carbon dioxide capture Values are approximate and measurement conditions differ between the cited studies.

Framework	Binding mechanism	Approximate BET area ($m^2\ g^{-1}$)	Approximate heat of adsorption (kJ mol^{-1})	Note
HKUST-1	Open Cu(II) sites	1500 to 1800	30 to 35	Loses capacity in humid gas [4,16]
UiO-66	Physisorption	1100 to 1400	25 to 30	Water stable, modest capacity [15]
Mg_2(dobdc)	Open Mg(II) sites	1400 to 1600	45 to 50	High dry capacity at 0.15 bar [10]
SIFSIX-3-Zn	Confined physisorption	Below 300	Around 45	Selectivity from pore geometry [8]
mmen-Mg_2(dobpdc)	Cooperative chemisorption	Around 3000 before grafting	Around 70	Stepped isotherm, tunable step [11,12]
CALF-20	Physisorption	Around 500	Around 38	Humidity tolerant, produced at scale [17]

4. WATER, COST AND THE SHIFT IN RESEARCH EMPHASIS

Water is the constraint that has removed most candidate materials from consideration. Flue gas leaving a desulphurisation unit is saturated, and at open metal sites water coordinates more strongly than carbon dioxide, so capacity collapses. Three responses have emerged. The first is to dry the feed, which imposes its own energy cost. The second is to use amine-appended frameworks, in which the carbamate chemistry proceeds in the presence of water and can even be assisted by it. The third is to seek frameworks whose pores exclude water on kinetic or thermodynamic grounds while still admitting carbon dioxide.

The last approach produced the clearest recent advance. A zinc triazolate oxalate framework of modest surface area retains its capacity in humid gas, tolerates repeated cycling, and can be synthesised in water from inexpensive reagents; it has been manufactured at tonne scale and tested in a commercial capture unit. [17] The material is unremarkable by the metrics that dominated the early literature and performs well by the ones that matter.

Computational screening has begun to contribute in the same direction. Large-scale simulation of hypothetical and reported structures, filtered on capacity under wet conditions rather than dry, identified candidate frameworks whose measured behaviour matched the prediction.[18] The value of these studies lies less in the specific materials proposed than in the demonstration that the screening criterion can be posed correctly in the first place.

Cost remains the least discussed obstacle. Linkers that require multistep synthesis, solvents that must be recovered, and activation procedures involving supercritical drying are acceptable in a laboratory and prohibitive in a plant that needs hundreds of tonnes of adsorbent. The materials most likely to be deployed are therefore not those with the highest reported capacities but those whose synthesis is short, aqueous and tolerant of impure feedstocks.

5. FROM POWDER TO PROCESS

An adsorbent is characterised as a powder and used as a shaped body in a contactor, and the translation between the two is where much reported performance is lost. Packed beds of loose crystallites give unacceptable pressure drop, so the material must be pelletised or supported, and binders occupy volume, block pores and can degrade the framework mechanically. Compression during shaping causes partial amorphisation in several well-known frameworks, with corresponding loss of capacity.

The cycle matters as much as the material. Temperature swing regeneration exploits the shift of the isotherm with temperature and suits strongly binding adsorbents, but heating and cooling a bed is slow and the thermal mass of the vessel is charged to the energy budget. Pressure or vacuum swing regeneration is faster and better suited to weakly binding materials, at the cost of compression work on a stream that is mostly nitrogen. Steam-assisted and combined swings are used where the adsorbent tolerates moisture. The stepped isotherms described in Section 2 are attractive in this context because they convert a small temperature change into a large change in loading, which is exactly the property a temperature swing needs.[9]

Comparison with the incumbent technology should therefore be made at the level of the process rather than the material. Aqueous amine scrubbing carries the penalty of heating a large volume of water, and a solid adsorbent avoids that penalty only if its own regeneration duty, the parasitic load of the blowers or vacuum pumps, and the cost of replacing degraded material together come to less.[1] Published assessments that quote uptake per gram without these terms are not comparable to the reference process.

Characterisation has kept pace with the chemistry. Diffraction on samples held under gas has located bound carbon dioxide within the pore, solid-state nuclear magnetic resonance has identified the carbamate species formed at appended amines, and calorimetry provides the heats of adsorption that isotherm fitting only estimates.[12,14] These measurements have removed a good deal of speculation about binding modes, and they are the reason the mechanisms in Section 2 can be stated with confidence.

6. CAPTURE FROM AMBIENT AIR

Removing carbon dioxide from air is the same separation with the partial pressure reduced by roughly a factor of four hundred. Adsorption at 0.0004 bar requires binding energies in the chemisorption range, since physisorbents that perform well on flue gas are almost empty at this pressure. Amine-functionalised frameworks and amine-loaded silicas are consequently the main candidates, and the design question shifts from capacity to the energy and the cycle time needed to recover a very dilute product.[19]

Two constraints dominate. Oxidative degradation of the amine limits lifetime, because ambient air supplies oxygen continuously at a temperature raised during regeneration. Mass transfer limits throughput, since moving the volume of air required to capture a tonne of carbon dioxide costs energy in proportion to the pressure drop across the contactor. Structured contactors with short diffusion paths address the second problem, and more oxidatively robust amines address the first, but neither is solved. Reported physisorbent approaches to direct capture remain limited to conditions where humidity is low.[20]

7. CONCLUSION

The chemistry of carbon dioxide capture in metal-organic frameworks is now well understood at the level of the individual binding site. Physisorption in tailored micropores, coordination at open metal centres and cooperative insertion at appended amines span a range of binding energies wide enough to match any realistic feed concentration, and the isotherm shape that each produces is predictable. The remaining difficulties are those of engineering and economics rather than of molecular design: tolerance of water, resistance to oxidation, mechanical integrity in a packed bed, and synthesis at a cost consistent with the value of the product. The recent appearance of a framework that is unremarkable in surface area yet manufacturable and humidity tolerant suggests that the field's criteria have adjusted accordingly, and that further progress will come from optimising against process conditions rather than against isotherm records.

REFERENCES

1. Rochelle GT. 2009. Amine scrubbing for CO2 capture. Science. 325(5948):1652–1654.
2. Yaghi OM, O'Keeffe M, Ockwig NW, Chae HK, Eddaoudi M, Kim J. 2003. Reticular synthesis and the design of new materials. Nature. 423(6941):705–714.
3. Li H, Eddaoudi M, O'Keeffe M, Yaghi OM. 1999. Design and synthesis of an exceptionally stable and highly porous metal-organic framework. Nature. 402(6759):276–279.
4. Chui SSY, Lo SMF, Charmant JPH, Orpen AG, Williams ID. 1999. A chemically functionalizable nanoporous material. Science. 283(5405):1148–1150.
5. Furukawa H, Ko N, Go YB, et al. 2010. Ultrahigh porosity in metal-organic frameworks. Science. 329(5990):424–428.
6. Millward AR, Yaghi OM. 2005. Metal-organic frameworks with exceptionally high capacity for storage of carbon dioxide at room temperature. J Am Chem Soc. 127(51):17998–17999.
7. Trickett CA, Helal A, Al-Maythalony BA, Yamani ZH, Cordova KE, Yaghi OM. 2017. The chemistry of metal-organic frameworks for CO2 capture, regeneration and conversion. Nat Rev Mater. 2:17045.
8. Nugent P, Belmabkhout Y, Burd SD, et al. 2013. Porous materials with optimal adsorption thermodynamics and kinetics for CO2 separation. Nature. 495(7439):80–84.
9. Bhatt PM, Belmabkhout Y, Cadiau A, et al. 2016. A fine-tuned fluorinated MOF for selective and efficient CO2 adsorption at low pressure. J Am Chem Soc. 138(29):9301–9307.
10. Caskey SR, Wong-Foy AG, Matzger AJ. 2008. Dramatic tuning of carbon dioxide uptake via metal substitution in a coordination polymer with cylindrical pores. J Am Chem Soc. 130(33):10870–10871.
11. McDonald TM, Mason JA, Kong X, et al. 2015. Cooperative insertion of CO2 in diamine-appended metal-organic frameworks. Nature. 519(7543):303–308.
12. Siegelman RL, McDonald TM, Gonzalez MI, et al. 2017. Controlling cooperative CO2 adsorption in diamine-appended Mg2(dobpdc) metal-organic frameworks. J Am Chem Soc. 139(30):10526–10538.
13. Mason JA, McDonald TM, Bae TH, et al. 2015. Application of a high-throughput analyzer in evaluating solid adsorbents for post-combustion carbon capture via multicomponent adsorption of CO2, N2, and H2O. J Am Chem Soc. 137(14):4787–4803.
14. Sumida K, Rogow DL, Mason JA, et al. 2012. Carbon dioxide capture in metal-organic frameworks. Chem Rev. 112(2):724–781.
15. Cavka JH, Jakobsen S, Olsbye U, et al. 2008. A new zirconium inorganic building brick forming metal organic frameworks with exceptional stability. J Am Chem Soc. 130(42):13850–13851.
16. Burtch NC, Jasuja H, Walton KS. 2014. Water stability and adsorption in metal-organic frameworks. Chem Rev. 114(20):10575–10612.
17. Lin JB, Nguyen TTT, Vaidhyanathan R, et al. 2021. A scalable metal-organic framework as a durable physisorbent for carbon dioxide capture. Science. 374(6574):1464–1469.
18. Boyd PG, Chidambaram A, García-Díez E, et al. 2019. Data-driven design of metal-organic frameworks for wet flue gas CO2 capture. Nature. 576(7786):253–256.
19. Sanz-Pérez ES, Murdock CR, Didas SA, Jones CW. 2016. Direct capture of CO2 from ambient air. Chem Rev. 116(19):11840–11876.
20. Kumar A, Madden DG, Lusi M, et al. 2015. Direct air capture of CO2 by physisorbent materials. Angew Chem Int Ed. 54(48):14372–14377.

INTERNATIONAL JOURNAL OF PURE SCIENCE RESEARCH STUDIES (IJPSRS)
(Open Access, Double-Blind Peer Reviewed Journal)
ISSN Online: 3139-8995



Amphibian Declines and Chytridiomycosis: Pathogen Biology, Impacts and Conservation Responses

Anjaly Jose

Assistant professor, Department of Zoology, Nirmalagiri College (Autonomous), Kerala, India

Article Information

Received: 28th July 2026
Received in revised form: 19th August 2026
Accepted: 21st September 2026
Available online: 4th November 2026

Volume: 2
Issue: 4
DOI: https://doi.org/10.63090/IJPSRS/3139.8995.0025

Abstract

Amphibians are declining faster than any other class of vertebrates, and a substantial part of that loss is attributable to a single group of fungal pathogens. This review covers the biology of the amphibian chytrids, the scale of the damage they have caused, and what conservation practice can and cannot do about it. Batrachochytrium dendrobatidis was described in 1999 after mass mortality events in Australia and Central America, and a second species specific to salamanders was described in 2013. Both infect keratinised skin, and the fungus kills by disrupting the transport of electrolytes across an organ that amphibians use for respiration and osmoregulation, leading to cardiac arrest. A global assessment associated the pathogen with declines in more than five hundred species, of which roughly ninety are presumed extinct, the largest documented loss of biodiversity attributable to a disease. Genomic evidence traces the hypervirulent lineage to east Asia and its global spread to the trade in live amphibians during the twentieth century. Outcomes vary with temperature, host skin peptides and skin bacterial communities, and a few populations have recovered without any decline in pathogen virulence. Effective measures remain limited to biosecurity, trade regulation and captive assurance colonies.

Keywords: Chytridiomycosis, Batrachochytrium, Amphibian Decline, Emerging Infectious Disease, Conservation

1. INTRODUCTION

Population losses among frogs and salamanders were first discussed as a general phenomenon in the late 1980s, and the pattern that puzzled field biologists was the disappearance of species from protected areas with intact habitat. The first global assessment concluded that nearly a third of amphibian species were threatened and that a large fraction of declines could not be explained by habitat loss or overexploitation .[1] Reassessment two decades later found the situation had not improved, with disease and climate change accounting for a growing share of deteriorations in status .[2]

The explanation for the unexplained cases emerged from work on mass mortality events in Queensland and Panama. Histological examination of dead and dying frogs revealed a chytrid fungus in the superficial layers of the skin, and the same organism was present at both sites on different continents .[3] It was formally described as Batrachochytrium dendrobatidis, the first chytrid known to parasitise a vertebrate .[4] A related species that attacks salamanders and newts, Batrachochytrium salamandrivorans, was described after mass mortality in Dutch fire salamander populations , and subsequent surveys traced its origin to Asian salamanders that carry it without severe disease .[5,6]

This paper reviews the biology of these pathogens, the evidence linking them to declines, the factors that determine whether an infected population persists, and the state of management.

2. PATHOGEN BIOLOGY AND LIFE CYCLE

The life cycle has two stages and is completed within days. A motile, uniflagellate zoospore swims in water, locates host skin, encysts and resorbs its flagellum. The resulting thallus develops within the epidermis into a zoosporangium, which matures and releases a new generation of zoospores through a discharge tube opening at the skin surface. Fig. 1 shows the sequence. In culture the cycle takes about four to five days at temperatures between 17 and 25 degrees Celsius .[7]

Thermal biology explains much of the epidemiology. Growth is optimal in the range just described, slows markedly above 28 degrees and stops near 30, so infected animals can clear the fungus by raising body temperature behaviourally, and outbreaks in the tropics concentrate at higher elevations and in cooler seasons. The salamander pathogen is adapted to cooler conditions still, with an optimum between 10 and 15 degrees, which shifts its risk zone towards temperate Europe and northern North America. Table 1 compares the two species.

Zoospores survive for a limited period in water without a host, and the fungus can persist on non-amphibian substrates and in tolerant host species. This reservoir capacity matters because it allows the pathogen to remain in a site after its most susceptible hosts have disappeared, which is why local extirpation of a species rarely leads to local elimination of the fungus.

Fig 1: Life cycle of the amphibian chytrid fungus, completed within days at temperatures favourable for growth .[4,7]

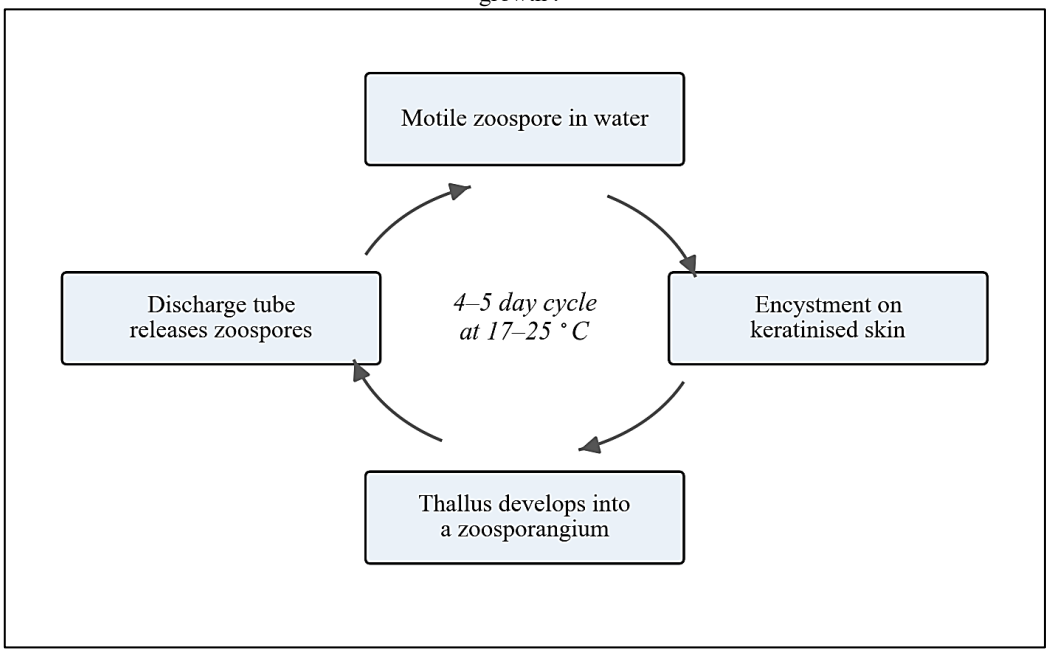


Table 1. Comparison of the two amphibian chytrid pathogens

Feature	B. dendrobatidis	B. salamandrivorans
First described	1999 [4]	2013 [5]
Principal hosts	Frogs, toads, some salamanders	Salamanders and newts
Growth optimum	17 to 25 °C	10 to 15 °C
Upper thermal limit	Near 30 °C	Near 25 °C
Inferred origin	East Asia [8]	East Asia [6]
Documented range	Global	Europe, with Asian reservoir

3. PATHOGENESIS

Amphibian skin performs functions that in other vertebrates are distributed among several organs. It contributes to gas exchange, regulates water balance and transports ions actively. Infection thickens and disorganises the epidermis, and the mechanism of death follows from that damage. Measurements in infected frogs showed reduced transport of sodium, potassium and chloride across the skin, progressive depletion of plasma electrolytes, and terminal cardiac arrest, with electrolyte supplementation delaying death .[9] Death is therefore a consequence of the loss of an osmoregulatory organ rather than of invasion of internal tissues, since the fungus does not penetrate beyond the epidermis.

The immune response is limited and in some respects suppressed. Susceptible species mount weak lymphocyte responses to infection, and fungal metabolites inhibit lymphocyte proliferation in culture, which may explain why heavy infections develop without effective clearance. Innate defences are more important:

antimicrobial peptides secreted by granular glands inhibit zoospores, and species whose peptide repertoires are more effective in vitro tend to persist better in the field.[10]

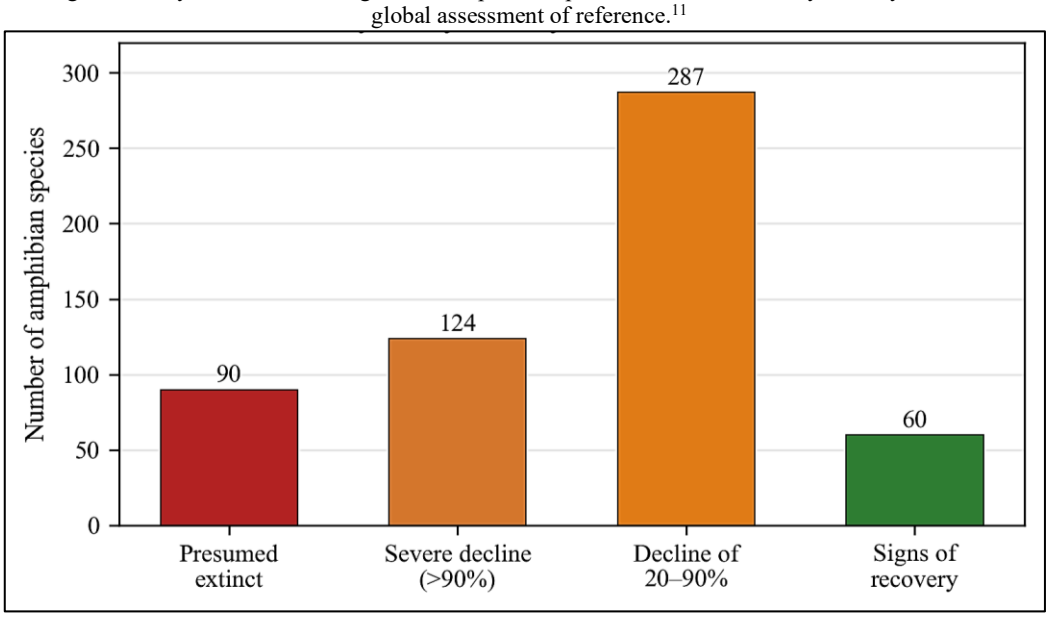
4. THE SCALE OF THE IMPACT

Quantifying the damage required assembling records that were scattered across regional literatures. A global synthesis identified 501 species with declines associated with chytridiomycosis. Of these, 90 are presumed extinct or extinct in the wild, a further 124 have declined by more than ninety percent, and about sixty show some evidence of recovery.[11] Fig. 2 shows the breakdown. The authors describe this as the greatest recorded loss of biodiversity attributable to a pathogen, and the concentration of losses in Central America, the Andes and eastern Australia reflects both the climate suitable for the fungus and the concentration of narrowly distributed montane species.

The pattern of arrival supports a causal reading rather than a coincidental one. In Panama, monitoring at a site before, during and after the arrival of the pathogen recorded a wave of mortality moving through the amphibian assemblage, with declines in the great majority of species over a single season.[12] Comparable wave-like spread was documented in Central America and Australia. Losses fell disproportionately on stream-associated and montane species, on those with narrow ranges and on those that were already rare.

These effects extend beyond the amphibians themselves. Loss of tadpoles changes algal communities and nutrient cycling in headwater streams, and snake assemblages that fed on frogs in affected Panamanian sites declined in abundance and diversity after their prey disappeared.

Fig 2: Severity of declines among the 50 amphibian species associated with chytridiomycosis in the global assessment of reference.[11]



5. ORIGINS AND SPREAD

The fungus was long suspected of being introduced rather than newly virulent, and genomic work settled the question. Sequencing of isolates worldwide identified several deeply divergent lineages, of which one, the global panzootic lineage, accounts for almost all outbreak-associated infections.[13] Expanded sampling located the greatest genetic diversity, and therefore the probable origin, in the Korean peninsula and adjacent parts of east Asia, and dated the emergence of the panzootic lineage to the early twentieth century, coinciding with the expansion of intercontinental trade in live amphibians.[8]

Two trade routes are implicated. The African clawed frog was exported in large numbers for pregnancy testing from the 1930s and carries the fungus with little disease. The American bullfrog is farmed for food and traded live across continents, and surveys of animals in trade regularly find infection. Both species tolerate infection well, which makes them effective carriers. The salamander pathogen followed the same pattern through the trade in Asian newts for the pet market.[6]

6. WHY SOME POPULATIONS PERSIST

Outcomes vary widely between species and between populations of the same species, and several factors contribute. Temperature is one, since populations in warm lowland sites experience conditions that limit fungal growth. Host defences are a second: differences in skin peptide composition correlate with survival.[10] A third is

the skin microbiome, since some resident bacteria produce antifungal metabolites, and experimental addition of such bacteria reduced mortality in laboratory trials.[14]

Evidence for recovery is genuine but modest. Populations of the mountain yellow-legged frog in California have increased at some sites despite continuing exposure, and the increase is associated with greater resistance among survivors rather than with the disappearance of the pathogen.[15] In Panama, an assemblage that had collapsed showed partial recovery, and experiments comparing archived and contemporary isolates found no reduction in virulence, which indicates that the change occurred in the hosts.[16] Recovery of this kind follows severe mortality and leaves populations smaller and less genetically diverse than before.

7. MANAGEMENT OPTIONS

Treatment of individual animals is straightforward, since antifungal agents and heat treatment clear infection reliably in captivity. Treating populations is not. Attempts to disinfect habitats or to treat wild animals at scale have succeeded only in small closed systems such as isolated ponds, and reinfection from reservoir hosts usually follows.[17]

Three approaches have practical value. Biosecurity in the field, including disinfection of boots and equipment between sites, slows human-assisted spread and costs little. Regulation of trade in live amphibians addresses the route by which both pathogens reached new continents, and import restrictions adopted in North America and Europe in response to the salamander pathogen represent the first case in which such a measure was taken before the pathogen arrived.[18] Captive assurance colonies preserve species that cannot currently survive in the wild, at high cost per species and with the unresolved problem of where such animals could eventually be released.

Approaches under investigation include bioaugmentation with protective bacteria, selection for resistance in captive stock, and vaccination using killed fungus or fungal fractions. None has yet produced durable protection under field conditions, and reviews of mitigation conclude that expectations should remain modest.[17,19]

8. SURVEILLANCE, DIAGNOSIS AND RISK ASSESSMENT

Everything described above depends on being able to detect infection reliably, and diagnosis was a limiting factor in the first decade of work. Histology of toe clips detects only heavy infections and requires killing or injuring the animal. The quantitative polymerase chain reaction assay developed for this pathogen changed both constraints: it works on a swab taken from the skin of a released animal, detects infections equivalent to a single zoospore, and returns a load estimate rather than a presence or absence call.[20] Load matters because mortality in most species follows a threshold, so a population carrying light infections is in a different situation from one approaching that threshold.

Two cautions apply to the resulting data. Swab results depend on sampling technique, on the season and on the body region sampled, so prevalence figures from different studies are not directly comparable. Inhibitors carried over from skin secretions and from environmental samples cause false negatives unless controls are included. Environmental sampling of water, which avoids handling animals altogether, is now common but detects the pathogen without indicating which host carries it.

Risk assessment for the salamander pathogen has been conducted largely in advance of its arrival in the Americas, which hold the greatest diversity of salamanders in the world. Susceptibility trials on North American species, combined with climate matching and with records of the newt trade, identified regions of the Appalachian mountains and the Pacific north west as areas where an introduction would be most damaging [18]. This assessment is the basis for the import restrictions mentioned in Section 7 and for targeted surveillance at ports of entry, an approach that reviews of the field regard as the most defensible use of limited resources.[19]

Climate change complicates both surveillance and prediction. Warming reduces the area suitable for the frog pathogen at low elevations while extending the season at high ones, and increases the frequency of temperature extremes that stress hosts without necessarily excluding the fungus. Because the outcome depends on the difference between host and pathogen thermal responses rather than on mean temperature, projections require both to be measured for the species in question, and these data exist for very few of them.

Host genetics has begun to inform both surveillance and captive management. Variation at major histocompatibility loci is associated with survival of infection in several frog species, with particular alleles more frequent among survivors after outbreaks and in populations that persist.[21] Screening for such markers offers a way to identify populations likely to withstand exposure and to avoid breeding out resistance in assurance colonies, where small founder numbers and selection for ease of husbandry both work against it. The association is statistical rather than deterministic, and resistance in the field also depends on skin peptides, microbiome and temperature, so marker-based selection supplements rather than replaces the measurement of survival under challenge.

9. CONCLUSION

Chytridiomycosis is the clearest case in which a single pathogen has driven losses of biodiversity at a global scale, and the sequence from discovery to explanation is unusually complete: the organism was identified, its pathogenesis established at the level of skin physiology, its origin traced by genomics and its spread linked to a specific human activity. What remains incomplete is the response. Effective intervention in wild populations is not available, and the measures that work, namely biosecurity and trade regulation, address future introductions rather than existing infections. The partial recoveries observed in California and Panama show that host populations can adapt, which is encouraging for species that retain sufficient numbers and genetic variation, and offers little to those that do not. Preventing the next introduction is the part of the problem where action is most likely to succeed.

REFERENCES

1. Stuart SN, Chanson JS, Cox NA, et al. Status and trends of amphibian declines and extinctions worldwide. Science. 2004;306(5702):1783–1786.
2. Luedtke JA, Chanson J, Neam K, et al. Ongoing declines for the world's amphibians in the face of emerging threats. Nature. 2023;622(7982):308–314.
3. Berger L, Speare R, Daszak P, et al. Chytridiomycosis causes amphibian mortality associated with population declines in the rain forests of Australia and Central America. Proc Natl Acad Sci USA. 1998;95(15):9031–9036.
4. Longcore JE, Pessier AP, Nichols DK. Batrachochytrium dendrobatidis gen. et sp. nov., a chytrid pathogenic to amphibians. Mycologia. 1999;91(2):219–227.
5. Martel A, Spitzen-van der Sluijs A, Blooi M, et al. Batrachochytrium salamandrivorans sp. nov. causes lethal chytridiomycosis in amphibians. Proc Natl Acad Sci USA. 2013;110(38):15325–15329.
6. Martel A, Blooi M, Adriaensen C, et al. Recent introduction of a chytrid fungus endangers Western Palearctic salamanders. Science. 2014;346(6209):630–631.
7. Piotrowski JS, Annis SL, Longcore JE. Physiology of Batrachochytrium dendrobatidis, a chytrid pathogen of amphibians. Mycologia. 2004;96(1):9–15.
8. O'Hanlon SJ, Rieux A, Farrer RA, et al. Recent Asian origin of chytrid fungi causing global amphibian declines. Science. 2018;360(6389):621–627.
9. Voyles J, Young S, Berger L, et al. Pathogenesis of chytridiomycosis, a cause of catastrophic amphibian declines. Science. 2009;326(5952):582–585.
10. Woodhams DC, Ardipradja K, Alford RA, Marantelli G, Reinert LK, Rollins-Smith LA. Resistance to chytridiomycosis varies among amphibian species and is correlated with skin peptide defenses. Anim Conserv. 2007;10(4):409–417.
11. Scheele BC, Pasmans F, Skerratt LF, et al. Amphibian fungal panzootic causes catastrophic and ongoing loss of biodiversity. Science. 2019;363(6434):1459–1463.
12. Lips KR, Brem F, Brenes R, et al. Emerging infectious disease and the loss of biodiversity in a Neotropical amphibian community. Proc Natl Acad Sci USA. 2006;103(9):3165–3170.
13. Farrer RA, Weinert LA, Bielby J, et al. Multiple emergences of genetically diverse amphibian-infecting chytrids include a globalized hypervirulent recombinant lineage. Proc Natl Acad Sci USA. 2011;108(46):18732–18736.
14. Harris RN, Brucker RM, Walke JB, et al. Skin microbes on frogs prevent morbidity and mortality caused by a lethal skin fungus. ISME J. 2009;3(7):818–824.
15. Knapp RA, Fellers GM, Kleeman PM, et al. Large-scale recovery of an endangered amphibian despite ongoing exposure to multiple stressors. Proc Natl Acad Sci USA. 2016;113(42):11889–11894.
16. Voyles J, Woodhams DC, Saenz V, et al. Shifts in disease dynamics in a tropical amphibian assemblage are not due to pathogen attenuation. Science. 2018;359(6383):1517–1519.
17. Garner TWJ, Schmidt BR, Martel A, et al. Mitigating amphibian chytridiomycoses in nature. Philos Trans R Soc Lond B Biol Sci. 2016;371(1709):20160207.
18. Yap TA, Koo MS, Ambrose RF, Wake DB, Vredenburg VT. Averting a North American biodiversity crisis. Science. 2015;349(6247):481–482.
19. Fisher MC, Garner TWJ. Chytrid fungi and global amphibian declines. Nat Rev Microbiol. 2020;18(6):332–343.
20. Boyle DG, Boyle DB, Olsen V, Morgan JAT, Hyatt AD. Rapid quantitative detection of chytridiomycosis (Batrachochytrium dendrobatidis) in amphibian samples using real-time Taqman PCR assay. Dis Aquat Organ. 2004;60(2):141–148.
21. Savage AE, Zamudio KR. MHC genotypes associate with resistance to a frog-killing fungus. Proc Natl Acad Sci USA. 2011;108(40):16705–16710.

INTERNATIONAL JOURNAL OF PURE SCIENCE RESEARCH STUDIES (IJPSRS)
(Open Access, Double-Blind Peer Reviewed Journal)
ISSN Online: 3139-8995
EDUSCHOOL ACADEMIC RESEARCH & PUBLISHERS



Total Stopping Times of the Collatz Map up to 10^7: A Computational Test of the Random-Walk Model

Lejo J Manavalan

Assistant Professor and Research Guide, Department of Mathematics, Little Flower College Guruvayur, Kerala, India

Article Information

Received: 22nd July 2026
Received in revised form: 25th August 2026
Accepted: 30th September 2026
Available online: 5th November 2026

Volume: 2
Issue: 4
DOI: https://doi.org/10.63090/IJPSRS/3139.8995.0026

Abstract

The Collatz or 3x + 1 conjecture asserts that repeated application of the map $T(n) = \frac{n}{2}$ for even n and $T(n) = \frac{(3n+1)}{2}$ for odd n eventually reaches 1 from every positive integer. Although unproven, it is supported by a heuristic random-walk model which predicts that the total stopping time σ(n), the number of iterations needed to reach 1, has mean approximately 6.952 ln n and a standard deviation proportional to √(ln n). This study computes σ(n) exactly for every integer up to 10^7 and tests these predictions. Trajectories were computed in C using memoisation and validated against direct iteration and known records. The longest trajectory below 10^7 begins at 8,400,511 and takes 429 steps of T (685 steps of the standard map), and the highest point reached, 3.02×10^{13}, occurs in the trajectory of 6,631,675. A least-squares fit of binned mean stopping times against ln n over 10^3 to 10^7 gives a slope of 6.817 ($R^2 = 0.9996$), within 2 per cent of the predicted 6.952. The variance of σ(n) grows in proportion to ln n, with a coefficient of 91 to 97 compared with the predicted 101.4. The standardised stopping times are close to Gaussian in the centre, with 68.7 per cent within one standard deviation, but are positively skewed, with skewness about 0.6 and a long right tail. The results support the random-walk model as a first approximation while identifying systematic departures in the variance and the tail.

Keywords: Collatz Conjecture, 3x + 1 Problem, Total Stopping Time, Random Walk, Stochastic Model, Experimental Mathematics, Dynamical Systems

1. INTRODUCTION

The Collatz problem, also known as the 3x + 1 problem, is one of the most famous unsolved problems in mathematics. Starting from a positive integer, one halves it if it is even and triples it and adds one if it is odd; the conjecture asserts that this process always eventually reaches 1.[1] Despite its elementary formulation, the problem has resisted proof, and it has become a test case for methods in number theory, dynamical systems and probability.[2]

Computational evidence for the conjecture is extensive: convergence has been verified for all starting values below 2^{68}.[3] On the theoretical side, Terras and Everett independently showed that almost all integers have a finite stopping time, in the sense that their trajectories eventually fall below their starting value,[4,5] and Tao proved that almost all orbits, in the sense of logarithmic density, attain almost bounded values.[6] A complete proof, however, remains out of reach.

An influential heuristic treats the parity sequence of a trajectory as if it were random, leading to a random-walk model for the logarithm of the iterates.[7,8] This model makes precise predictions about the statistics of the

total stopping time, but these predictions are not theorems. This study tests them against exact computation. Its objectives are:

- To compute the total stopping time of every integer up to 10^7;
- To identify extreme trajectories in this range;
- To compare the growth of the mean and variance of stopping times with the model's predictions; and
- To examine the shape of the distribution of standardised stopping times.

2. LITERATURE REVIEW

2.1. Definitions

Following common practice, we use the accelerated map[1,3]

$$T(n) = \frac{n}{2} \text{ if n is even;} \quad T(n) = \frac{3n+1}{2} \text{ if n is odd,} \tag{1}$$

which combines each odd step with the halving that necessarily follows it. The total stopping time of n is

$$\sigma(n) = \min \{ k \geq 0 : T^k(n) = 1 \}, \tag{2}$$

and the stopping time is the least k such that $T^k(n) < n$. The number of steps of the standard map, in which 3n + 1 and halving are counted separately, equals σ(n) plus the number of odd steps.

2.2. The Random-Walk Model

If the parity of successive iterates is treated as a sequence of independent fair coin tosses, each application of T multiplies the current value by approximately $\frac{3}{2}$ or $\frac{1}{2}$ with equal probability. The logarithm of the iterate then performs a random walk with increments $\ln\left(\frac{3}{2}\right)$ *and* $\ln\left(\frac{1}{2}\right)$, *whose mean is*

$$m = \frac{1}{2}\ln\left(\frac{3}{4}\right) \approx -0.14384 \tag{3}$$

and whose variance is $v = \frac{(\ln 3)^2}{4} \approx 0.30174$. The expected time for the walk to descend from ln n to 0 is $\frac{\ln n}{|m|}$, giving the prediction[8,7]

$$E[\sigma(n)] \approx \mu \ln n, \qquad \mu \frac{2}{\ln(4/3)} \approx 6.9521 \tag{4}$$

Standard results on first-passage times of random walks further imply that the variance of the passage time grows as $\frac{v \ln n}{|m|^3}$, so that

$$\text{var}[\sigma(n)] \approx \kappa \ln n, \quad \kappa = \frac{v}{|m|^3} \approx 101.39 \tag{5}$$

and that the standardised total stopping time is approximately normally distributed.[8] Crandall gave an early heuristic analysis of this kind,[9] and Lagarias and Weiss developed rigorous versions of stochastic models for the problem.[7] Kontorovich and Lagarias emphasised that these models generate conjectures rather than proofs, and that nothing has been rigorously proved about the average size of the total stopping time.[8] Systematic comparisons of the model's predictions for the mean, variance and distribution with exact data over a large range are therefore of interest.

3. METHODS

3.1. Computation

The total stopping time σ(n), the number of odd steps and the largest value attained were computed for every n from 1 to $N = 10^7$ in the C programming language using memoisation. For each n, the trajectory under T was followed only until it first fell below n, at which point the previously computed values for the smaller number were added. Because the stopping time is finite for every n in the range, this procedure yields σ(n) for all n in increasing order. Values were stored as 16-bit integers for stopping times and 64-bit integers for maxima, and the computation required less than one second. Statistical analysis was carried out in Python with NumPy.[10]

3.2. Validation

The memoised results were checked against direct iteration of T for n = 2, 3, 7, 27, 97, 871, 837,799, 8,400,511 and 9,999,999, with exact agreement. The trajectory of 27 requires 70 steps of T, or 111 steps of the

standard map, and reaches a maximum of 4,616 under T, corresponding to 9,232 under the standard map, in agreement with well-known values. The standard-map step counts for the record holders 837,799 (524 steps) and 8,400,511 (685 steps) also agree with established results.

3.3. Statistical Comparison

To estimate the growth rate of the mean, the range 10^3 to 10^7 was divided into 40 intervals of equal logarithmic width, and the mean of σ(n) in each interval was regressed on the mean of ln n by least squares. The variance was examined in five windows, $[10^3, 2 \times 10^3)$, $[10^4, 2 \times 10^4)$, $[10^5, 2 \times 10^5)$, $[10^6, 2 \times 10^6)$ and $[5 \times 10^6, 10^7)$, by computing Var σ(n)/E[ln n]. Finally, standardised stopping times

$$z = \frac{\sigma(n) - \mu \ln n}{\sqrt{\kappa \ln n}} \tag{6}$$

were computed for $5 \times 10^6 \leq n \leq 10^7$ and their distribution was compared with the standard normal.

4. RESULTS

4.1. Extreme Trajectories

Every integer up to 10^7 reaches 1, consistent with earlier verification.[3] Table 1 lists notable trajectories. The largest total stopping time below 10^7 is attained by n = 8,400,511, with 429 steps of T (685 of the standard map), and the largest below 10^6 by 837,799, with 329 steps of T (524 of the standard map). The highest value reached by any trajectory starting below 10^7 is 30,171,305,459,816 under T, attained from n = 6,631,675; under the standard map this corresponds to 60,342,610,919,632. The largest stopping time, that is, the longest time before first falling below the starting value, is 246 steps, attained by n = 8,088,063. There are 54 delay records, integers whose total stopping time exceeds that of every smaller integer, up to 10^7.

Table 1: Notable trajectories of the Collatz map for $n \leq 10^7$

n	σ(n), steps of T	Odd steps	Standard-map steps	Stopping time	Maximum under T
27	70	41	111	59	4,616
837,799	329	195	524	105	1,487,492,288
6,631,675	362	214	576	222	30,171,305,459,816
8,088,063	356	210	566	246	8,077,577,336
8,400,511	429	256	685	214	79,712,307,440

Source: Author's computation. 837,799 and 8,400,511 have the largest total stopping times below 10^6 and 10^7; 6,631,675 reaches the highest maximum and 8,088,063 has the largest stopping time below 10^7.

4.2. Growth of the Mean

Figure 1(a) shows σ(n) for a sample of n up to 10^7 together with the curve 6.952 ln n. The least-squares regression of binned means on ln n gives a slope of 6.817 and an intercept of 0.51, with $R^2 = 0.9996$. The fitted slope is 1.9 per cent below the predicted value μ = 6.952. In the window $5 \times 10^6 \leq n \leq 10^7$, σ(n) falls short of μ ln n by 1.40 steps on average. The mean of σ(n) over all $n \leq 10^7$ is 103.7 steps. Table 2 shows that the ratio of σ(n) to ln n remains between 6.84 and 6.86 across windows from 10^3 to 10^7.

Table 2: Statistics of total stopping times in selected windows compared with the random-walk model

Window	Mean σ(n)/ln n	Var σ(n)/ln n	Mean Z	SD of Z	Skewness of Z
$10^3 – 2 \times 10^3$	6.842	96.6	−0.030	0.976	0.53
$10^4 – 2 \times 10^4$	6.859	91.0	−0.029	0.946	0.51
$10^5 – 2 \times 10^5$	6.844	90.9	−0.037	0.946	0.57
$10^6 – 2 \times 10^6$	6.857	91.8	−0.036	0.951	0.62
$5 \times 10^6 – 10^7$	6.863	92.6	−0.035	0.955	0.64
Model prediction	6.952	101.4	0	1	—

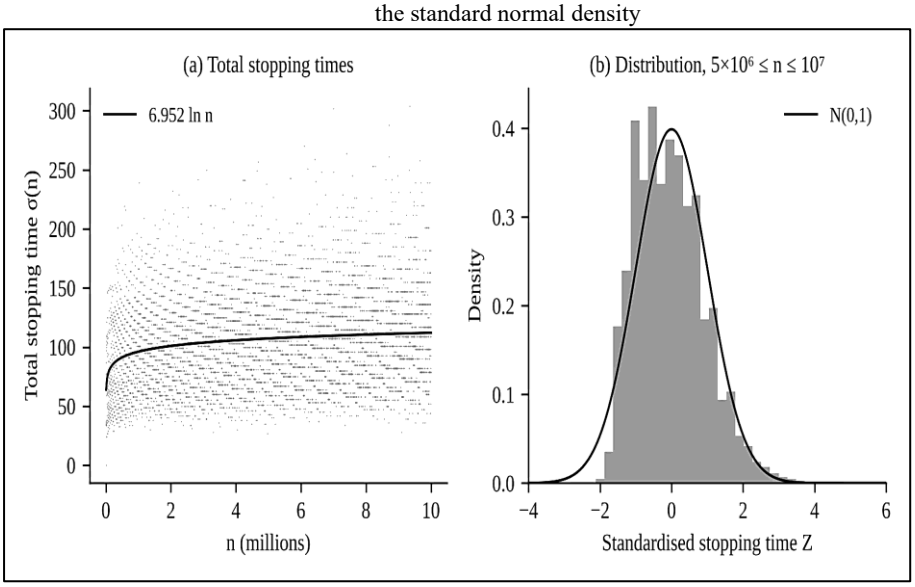
Source: Author's computation. $z = \frac{\sigma(n) - \mu \ln n}{\sqrt{\kappa \ln n}}$ *with μ = 6.952 and κ = 101.39 from Equations (4) and (5).*

4.3. Variance and Distribution

The variance of σ(n) grows approximately in proportion to ln n, as the model predicts, but with a smaller coefficient. Across the five windows, Var σ(n)/ln n lies between 90.9 and 96.6, about 5 to 10 per cent below the predicted κ = 101.39 (Table 2). Consequently, the standard deviation of the standardised variable Z is about 0.95 rather than 1.

Figure 1(b) compares the distribution of Z for $5 \times 10^6 \leq n \leq 10^7$ with the standard normal density. The centre of the distribution is close to Gaussian: 68.7 per cent of values lie within one unit of zero, compared with 68.3 per cent for a normal distribution. However, the distribution is markedly asymmetric. Its skewness is about 0.6, and its range extends from −2.18 to 7.91, so that the right tail is much longer than the left. The fraction of values within two units of zero is 97.0 per cent, higher than the normal 95.4 per cent, reflecting the truncated left tail.

Figure 1: (a) Total stopping times σ(n) for a sample of $n \leq 10^7$ with the predicted mean 6.952 ln n; (b) distribution of standardised stopping times for $5 \times 10^6 \leq n \leq 10^7$ compared with the standard normal density



Source: Author's computation. Panel (a) shows every 997th integer; panel (b) uses every fifth integer in the window.

4.4. Stopping Times

The distribution of stopping times follows the simple parity structure of the map. Exactly half of all integers greater than 1, the even ones, have stopping time 1; 75 per cent have stopping time at most 2; and 87.5 per cent at most 5. The proportions with stopping time at most 10 and 20 are 93.75 and 97.39 per cent respectively. These values reflect the fact that the stopping time is determined by the residue of n modulo powers of 2, as shown by Terras.[4]

5. DISCUSSION

The results provide substantial support for the random-walk model as a description of Collatz trajectories, while revealing systematic departures that deserve attention.

First, the predicted logarithmic growth of the mean is clearly confirmed, and the fitted slope agrees with the predicted constant to within 2 per cent. The small shortfall, together with the negative offset of about 1.4 steps, is consistent with boundary effects near the end of a trajectory: the model treats the descent to 1 as a continuous random walk, whereas real trajectories terminate deterministically through small values such as 16, 8, 4, 2 and 1, where the parity sequence is fixed rather than random.

Second, the variance grows in proportion to ln n, as predicted, but is about 9 per cent smaller than the model suggests. One possible explanation is that the parity sequences of Collatz trajectories are not fully independent. For example, after an odd step $\frac{3n+1}{2}$, the parity of the next iterate is determined by the residue of n modulo 4, so long runs of particular parities are constrained by congruence conditions. Such dependence can reduce variability relative to independent coin tossing.

Third, the distribution of standardised stopping times is positively skewed with a long right tail, as expected of first-passage times, which cannot be much smaller than the minimum number of halvings required but can be much larger when a trajectory makes a long excursion. The model's Gaussian limit applies as ln n →

∞, but because ln n grows so slowly, the range 10^7 corresponds to ln n ≈ 16, far from the asymptotic regime. The skewness observed here did not decrease between 10^3 and 10^7, suggesting that convergence to normality, if it occurs, is very slow.

These observations do not bear directly on the truth of the conjecture, which concerns every trajectory rather than typical ones. They show, however, that the heuristic picture that underlies belief in the conjecture accurately captures the typical behaviour of trajectories, while its quantitative predictions for variance and tails need refinement.

6. CONCLUSION

This study has computed the total stopping time of the Collatz map for every integer up to 10^7 and compared the results with the random-walk model. All trajectories reach 1. The mean total stopping time grows as 6.817 ln n, within 2 per cent of the predicted 6.952 ln n, and the variance grows in proportion to ln n with a coefficient about 9 per cent below the prediction. The standardised stopping times are near-Gaussian in the centre but positively skewed, with a long right tail.

Future work could:

- Extend the computation to 10^{10} or beyond to track the convergence of the variance coefficient and skewness;
- Develop refined stochastic models that incorporate dependence between successive parities and boundary effects near 1;
- Compare the results with the 5x + 1 map, for which the model predicts divergent trajectories; and
- Analyse the distribution of the maximum excursion of trajectories.

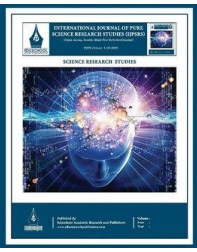
ACKNOWLEDGMENTS

[Add acknowledgments.] Conflict of interest: none declared. Funding: none received. Data availability: the code used for the computations can be provided by the authors on request. Use of artificial intelligence: the author(s) used Claude (Anthropic) to assist with computation, literature exploration and drafting; all computations, results and references were checked by the author(s), who take full responsibility for the manuscript.

REFERENCES

1. Lagarias JC. 1985. The 3x+1 problem and its generalizations. Am Math Monthly. 92(1):3–23.
2. Lagarias JC, editor. 2010. The ultimate challenge: the 3x+1 problem. Providence (RI): American Mathematical Society.
3. Bařina D. 2021. Convergence verification of the Collatz problem. J Supercomput. 77(3):2681–2688. doi:10.1007/s11227-020-03368-x.
4. Terras R. 1976. A stopping time problem on the positive integers. Acta Arith. 30(3):241–252.
5. Everett CJ. 1977. Iteration of the number-theoretic function f(2n) = n, f(2n + 1) = 3n + 2. Adv Math. 25(1):42–45.
6. Tao T. 2022. Almost all orbits of the Collatz map attain almost bounded values. Forum Math Pi. 10:e12. doi:10.1017/fmp.2022.8.
7. Lagarias JC, Weiss A. 1992. The 3x+1 problem: two stochastic models. Ann Appl Probab. 2(1):229–261. doi:10.1214/aoap/1177005779.
8. Kontorovich AV, Lagarias JC. 2009. Stochastic models for the 3x + 1 and 5x + 1 problems. arXiv:0910.1944 [math.NT].
9. Crandall RE. 1978. On the '3x + 1' problem. Math Comp. 32(144):1281–1292.
10. Harris CR, Millman KJ, van der Walt SJ, Gommers R, Virtanen P, Cournapeau D, Wieser E, Taylor J, Berg S, Smith NJ, et al. 2020. Array programming with NumPy. Nature. 585(7825):357–362. doi:10.1038/s41586-020-2649-2.

INTERNATIONAL JOURNAL OF PURE SCIENCE RESEARCH STUDIES (IJPSRS)
(Open Access, Double-Blind Peer Reviewed Journal)
ISSN Online: 3139-8995



Magnetoreception and Navigation in Migratory Animals: Mechanisms and Evidence

Jeeva Chacko

Principal, Department of Zoology, St. Mary's Arts and Science College, Cherupanathady, Kerala, India

Article Information

Received: 27th July 2026
Received in revised form: 29th August 2026
Accepted: 1st October 2026
Available online: 5th November 2026

Volume: 2
Issue: 4
DOI: https://doi.org/10.63090/IJPSRS/3139.8995.0027

Abstract

Animals as different as songbirds, sea turtles, salmon and butterflies reach destinations they have never seen, and part of the information they use comes from the geomagnetic field. This review separates the two capacities involved, a compass that reads direction and a map that estimates position, and examines the evidence for each. Behavioural work in orientation cages established that the avian compass responds to the inclination of field lines rather than to their polarity, that it requires light of short wavelength, and that it is disrupted by weak radio-frequency fields. These properties point to a quantum mechanism in which a light-induced radical pair interconverts between singlet and triplet states at a rate that depends on the orientation of the molecule in the field, and cryptochrome proteins from the retina of a migratory songbird show magnetic sensitivity in vitro. A second mechanism based on biogenic magnetite is supported by conditioning experiments and by trigeminal recordings, though the cells once identified as receptors in the pigeon beak proved to be macrophages. Displacement experiments in reed warblers, sea turtles and salmon indicate a magnetic map based on inclination and declination. No receptor has been confirmed in any species.

Keywords: Magnetoreception, Radical Pair, Cryptochrome, Magnetite, Animal Navigation

1. INTRODUCTION

Long-distance migration presents an orientation problem that improves little with experience for the individuals that most need to solve it. Many songbirds migrate alone and at night on their first journey, without parental guidance, and arrive in a wintering area used by their species. Sea turtles hatch on a beach, spend years at sea, and return to nest within tens of kilometres of their natal site. Solving such problems requires directional information and, for the return leg, some estimate of position.

Animals use several cues in combination, including the position of the sun, the pattern of polarised light at dusk, the rotation of the star field, olfactory gradients and landmarks. The geomagnetic field is distinctive among them because it is available at all times, in all weather, and at any depth or altitude. Its usefulness was established when European robins tested in orientation cages under a controlled artificial field oriented according to that field rather than to any visual cue .[1]

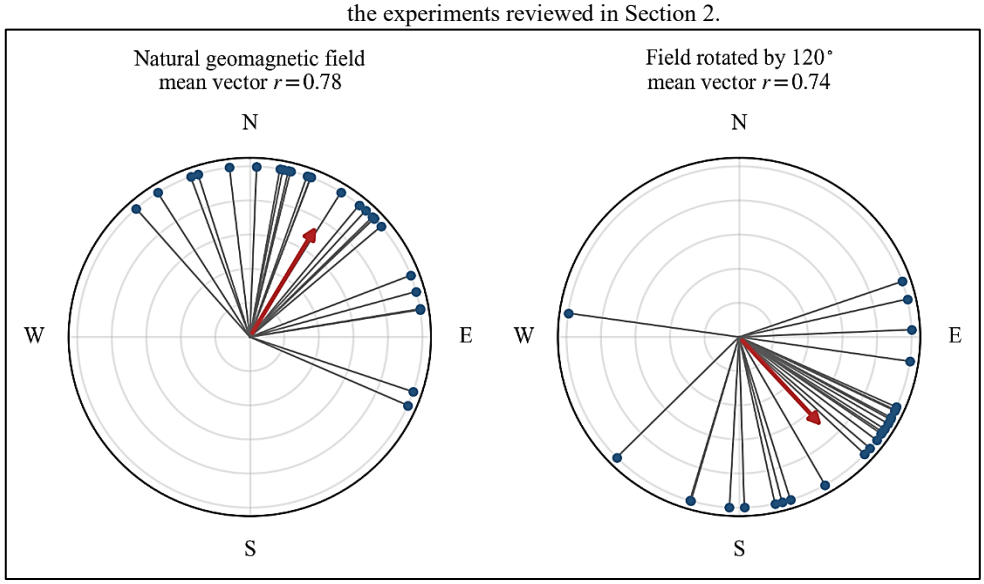
Two capacities must be distinguished. A compass converts a field into a direction. A map converts local field values into an estimate of position relative to a goal, which requires the animal to compare measurements against learned or inherited reference values. The two need not share a receptor, and current evidence suggests they do not. This review examines each in turn, then considers what remains unresolved .[2]

2. THE COMPASS AND HOW IT IS MEASURED

Most behavioural evidence comes from orientation cages of the type introduced by Emlen and Emlen, in which a bird in migratory condition hops on an inked or scratch-sensitive surface and leaves a record of its preferred heading .[3] Headings from many individuals are analysed by circular statistics, and the length of the mean vector measures how concentrated they are. Fig. 1 illustrates the logic: when the ambient field is rotated, headings rotate with it, which demonstrates that the birds are reading the field rather than an uncontrolled cue.

The avian compass has three properties that constrain any mechanism proposed for it. First, it responds to the inclination of the field lines relative to gravity and not to their polarity, so it distinguishes poleward from equatorward rather than north from south. Second, it requires light, and it works under short-wavelength illumination but fails under long-wavelength light. Third, it is disrupted by oscillating fields in the megahertz range that are far weaker than the geomagnetic field itself .[4] The last property is the most diagnostic, since a simple magnetic particle would be unaffected by such a weak oscillating field, while a system whose behaviour depends on electron spin would not.

Fig 1: Orientation-cage logic. Each line marks the heading of one individual and the arrow shows the mean vector. When the ambient field is rotated, the distribution rotates with it, as reported in the experiments reviewed in Section 2.



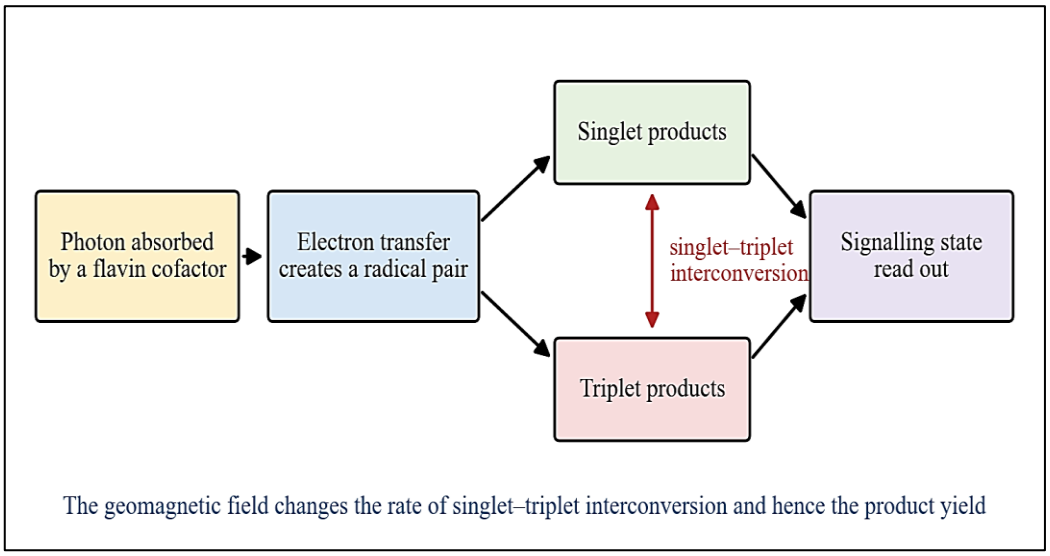
3. THE RADICAL-PAIR MECHANISM

Ritz, Adem and Schulten proposed that the light-dependent compass operates through a photochemical reaction producing a pair of radicals whose unpaired electron spins are initially correlated .[5] The pair interconverts between singlet and triplet configurations, and the rate of interconversion depends on the angle between the molecule and the external field, because hyperfine coupling to nearby nuclei makes the spin dynamics anisotropic. Since the two configurations yield different chemical products, the yield becomes a function of orientation. Fig. 2 shows the scheme. The mechanism explains all three behavioural properties at once: it requires light to create the radical pair, it is insensitive to polarity because the axis and not the direction matters, and it is disrupted by radio-frequency fields tuned near the electron spin transitions .[6]

Cryptochromes are the candidate molecules. They are flavoproteins present in the retina, and light absorption by the flavin cofactor produces a radical pair through a chain of electron transfers along conserved tryptophan residues. Purified cryptochrome 4 from the European robin responds to applied magnetic fields in vitro, and the response is weaker in the corresponding proteins from non-migratory chicken and pigeon, which is the closest link so far between the molecule and the behaviour .[7] The magnetic effects observed in isolated protein are nevertheless produced by fields stronger than the geomagnetic one, and how the sensitivity is amplified in the intact retina is unknown.

Neuroanatomy supports a visual pathway. Lesion experiments in European robins showed that birds without a functioning trigeminal nerve still orient by the magnetic compass, while lesions to a forebrain region called cluster N, which receives input from the eyes and is active during night-time orientation, abolish the ability .[8] Tracing studies confirm that this region is connected to the retina through the thalamofugal pathway .[9] The compass therefore appears to be a visual function in birds, a conclusion consistent with reports that low-frequency electromagnetic noise in urban environments disrupts orientation and that shielded huts restore it .[10]

Fig 2: The radical-pair scheme proposed for the light-dependent compass .[5,6] Product yields depend on the orientation of the molecule relative to the field.



4. MAGNETITE-BASED RECEPTION

A second mechanism uses crystals of biogenic magnetite, which experience a torque in an external field that could be transduced by mechanoreceptors .[11] Unlike the radical-pair system this mechanism is sensitive to polarity and does not require light, so it is the natural candidate for a map sense that must measure field intensity.

The evidence is mixed. Conditioning experiments show that pigeons can be trained to discriminate magnetic anomalies, and that this ability depends on the trigeminal nerve and on an intact upper beak .[12] Recordings from the pigeon brainstem identified neurons whose firing encoded field direction and intensity .[13] Against this, the iron-rich cells in the upper beak that were widely reported as candidate receptors were shown by systematic histology to be macrophages rather than neurons, a result that removed the main anatomical support for the model .[14]

The current position is that behavioural and electrophysiological evidence for a magnetite-based sense is reasonably strong while the cellular identification is absent. The receptor may be rare, small and distributed, which would explain the difficulty. As one review put the matter, this is a sense without a known receptor .[15]

5. EVIDENCE FOR A MAGNETIC MAP

Position sensing requires at least two independent field parameters that vary in different directions. Inclination and total intensity vary mainly with latitude, while declination, the angle between magnetic and geographic north, varies with longitude in many regions. Displacement experiments provide the key evidence. Eurasian reed warblers displaced eastwards by more than a thousand kilometres corrected their heading appropriately, and birds held in a field where only declination was altered behaved as if displaced along the longitude that the altered declination implied.[16] A later study showed that the same species extrapolates beyond the range of values it has experienced, which implies a gradient map rather than a memorised set of local values .[17]

Marine examples are equally instructive. Hatchling loggerhead turtles placed in fields replicating locations around their oceanic migration route swam in directions appropriate to each location, indicating inherited responses to regional field values .[18] Analysis of nesting records showed that turtles return to beaches whose field signature matches that of their natal site, and that gradual drift of the geomagnetic field is accompanied by corresponding shifts in nesting distributions, which supports imprinting on a magnetic signature .[19] In Pacific salmon, juveniles with no prior ocean experience oriented according to fields representing the northern and southern edges of their range, again indicating an inherited map .[20] Monarch butterflies possess a light-dependent inclination compass, demonstrating that the mechanism is not confined to vertebrates .[21] Table 1 summarises the evidence by mechanism.

Magnetic information is never used alone. Birds recalibrate their magnetic compass against the pattern of polarised light near sunset, and the direction of that calibration differs between species and seasons. Olfactory cues contribute to homing in pigeons and to navigation in seabirds, and experienced individuals rely more on learned landmarks than first-year migrants can. The hierarchy among cues shifts with conditions, which is one reason that removing a single cue in an experiment often produces a smaller effect than the importance of that cue would suggest .[2] Interpreting negative results in this field therefore requires care, since redundancy between systems can mask the loss of any one of them.

Table 1. Evidence for the two proposed magnetoreception mechanisms

Property	Radical pair	Magnetite
Requires light	Yes	No
Sensitive to polarity	No, reads inclination	Yes
Disrupted by radio-frequency fields	Yes [4,6]	Not expected
Candidate molecule identified	Cryptochrome 4 [7]	Biogenic magnetite [11]
Neural pathway	Visual, via cluster N [8,9]	Trigeminal [12,13]
Receptor cell confirmed	No	No, earlier claim withdrawn [14]
Proposed role	Compass	Map and intensity detection

6. MAGNETIC RESPONSES BEYOND BIRDS

Attention to birds reflects the convenience of the orientation cage rather than any restriction of the sense. Comparable evidence exists across vertebrates and in several invertebrate groups.

Bats calibrate their homing direction against the magnetic field. Big brown bats displaced from their roost and exposed to a rotated field at sunset departed in directions rotated accordingly, which indicates that the field is used together with a cue available at dusk.[22] Subterranean mole rats, which live in complete darkness and cannot use celestial cues at all, build nests in a preferred magnetic direction and reverse that preference when the field is reversed; their compass responds to polarity rather than inclination and does not require light, so it is unlikely to share a mechanism with the avian system.[23]

Spontaneous alignment provides a different class of evidence. Analysis of satellite images and field observations found that cattle and deer at rest tend to align along the magnetic north to south axis, an effect that weakened near power lines where the field is distorted.[24] Alignment of this kind carries no obvious navigational function and is best treated as an indication that the field is perceived rather than as evidence of a compass in use.

Among invertebrates the monarch butterfly has a light-dependent inclination compass with the same spectral dependence as the avian system, and social insects, spiny lobsters and several molluscs respond to field manipulation.[21] The distribution of the trait across such distant lineages suggests either an ancient origin or repeated independent evolution, and the mechanistic differences between the avian and the mole rat compasses favour the second interpretation.

7. UNRESOLVED PROBLEMS

Three difficulties stand out. The first is the sensitivity gap. Magnetic effects on isolated cryptochrome require fields well above geomagnetic strength, and the behavioural sensitivity of birds implies that the biological system detects changes of a few percent in a field of about fifty microtesla. Proposed solutions involve ordered arrays of receptor molecules and long-lived spin coherence, but neither has been demonstrated in a retina.

The second is replication. Several influential results in this field have proved difficult to reproduce across laboratories, and the effects are small relative to individual variation in orientation behaviour. Sample sizes in cage experiments are often modest, and the analysis depends on circular statistics whose assumptions are not always checked. Reports of disruption by anthropogenic electromagnetic noise are important for this reason as well as for their conservation implications, since they suggest that ambient conditions in the laboratory may themselves influence outcomes .[10]

The third is the receptor. No cell has been identified in any species that responds to magnetic stimuli and projects to the brain, in contrast with every other sensory modality. The nearest approach came from rainbow trout, where cells containing magnetite were located in the olfactory lamellae and units in the associated branch of the trigeminal nerve responded to changes in field intensity ; the identification has proved difficult to extend to other species, and isolating candidate cells from surrounding tissue remains the main technical obstacle.[25] Until such a cell is described completely, mechanistic accounts remain inferences from behaviour and biochemistry rather than descriptions of a sensory system.

8. CONCLUSION

Magnetic orientation is established beyond reasonable doubt in birds, turtles, salmon and several insects, and the properties of the avian compass constrain its mechanism tightly enough to make the radical-pair proposal the leading explanation. Magnetite-based detection remains the more plausible basis for measuring intensity and hence for the map sense, despite the loss of its principal anatomical evidence. Displacement experiments show that the map uses at least two field parameters and that animals extrapolate from them rather than matching

remembered values. The outstanding requirement is cellular: identification of a receptor and of its afferent pathway would convert a well-supported inference into a described sense, and would also clarify how far anthropogenic fields interfere with migration.

REFERENCES

1. Wiltschko W, Wiltschko R. 1972. Magnetic compass of European robins. Science. 176(4030):62–64.
2. Mouritsen H. 2018. Long-distance navigation and magnetoreception in migratory animals. Nature. 558(7708):50–59.
3. Emlen ST, Emlen JT. 1966. A technique for recording migratory orientation of captive birds. Auk. 83(3):361–367.
4. Ritz T, Thalau P, Phillips JB, Wiltschko R, Wiltschko W. 2004. Resonance effects indicate a radical-pair mechanism for avian magnetic compass. Nature. 429(6988):177–180.
5. Ritz T, Adem S, Schulten K. 2000. A model for photoreceptor-based magnetoreception in birds. Biophys J. 78(2):707–718.
6. Hore PJ, Mouritsen H. 2016. The radical-pair mechanism of magnetoreception. Annu Rev Biophys. 45:299–344.
7. Xu J, Jarocha LE, Zollitsch T, et al. 2021. Magnetic sensitivity of cryptochrome 4 from a migratory songbird. Nature. 594(7864):535–540.
8. Zapka M, Heyers D, Hein CM, et al. 2009. Visual but not trigeminal mediation of magnetic compass information in a migratory bird. Nature. 461(7268):1274–1277.
9. Heyers D, Manns M, Luksch H, Güntürkün O, Mouritsen H. 2007. A visual pathway links brain structures active during magnetic compass orientation in migratory birds. PLoS One. 2(9).
10. Engels S, Schneider NL, Lefeldt N, et al. 2014. Anthropogenic electromagnetic noise disrupts magnetic compass orientation in a migratory bird. Nature. 509(7500):353–356.
11. Kirschvink JL, Walker MM, Diebel CE. 2001. Magnetite-based magnetoreception. Curr Opin Neurobiol. 11(4):462–467.
12. Mora CV, Davison M, Wild JM, Walker MM. 2004. Magnetoreception and its trigeminal mediation in the homing pigeon. Nature. 432(7016):508–511.
13. Wu LQ, Dickman JD. 2012. Neural correlates of a magnetic sense. Science. 336(6084):1054–1057.
14. Treiber CD, Salzer MC, Riegler J, et al. 2012. Clusters of iron-rich cells in the upper beak of pigeons are macrophages not magnetosensitive neurons. Nature. 484(7394):367–370.
15. Nordmann GC, Hochstoeger T, Keays DA. 2017. Magnetoreception: a sense without a receptor. PLoS Biol. 15(10).
16. Chernetsov N, Pakhomov A, Kobylkov D, Kishkinev D, Holland RA, Mouritsen H. 2017. Migratory Eurasian reed warblers can use magnetic declination to solve the longitude problem. Curr Biol. 27(17):2647–2651.
17. Kishkinev D, Packmor F, Zechmeister T, et al. 2021. Navigation by extrapolation of geomagnetic cues in a migratory songbird. Curr Biol. 31(7):1563–1569.
18. Lohmann KJ, Lohmann CMF, Putman NF. 2007. Magnetic maps in animals: nature's GPS. J Exp Biol. 210(21):3697–3705.
19. Brothers JR, Lohmann KJ. 2015. Evidence for geomagnetic imprinting and magnetic navigation in the natal homing of sea turtles. Curr Biol. 25(3):392–396.
20. Putman NF, Scanlan MM, Billman EJ, et al. 2014. An inherited magnetic map guides ocean navigation in juvenile Pacific salmon. Curr Biol. 24(4):446–450.
21. Guerra PA, Gegear RJ, Reppert SM. 2014. A magnetic compass aids monarch butterfly migration. Nat Commun. 5:4164.
22. Holland RA, Thorup K, Vonhof MJ, Cochran WW, Wikelski M. 2006. Bat orientation using Earth's magnetic field. Nature. 444(7120):702.
23. Marhold S, Wiltschko W, Burda H. 1997. A magnetic polarity compass for direction finding in a subterranean mammal. Naturwissenschaften. 84(9):421–423.
24. Begall S, Cerveny J, Neef J, Vojtech O, Burda H. 2008. Magnetic alignment in grazing and resting cattle and deer. Proc Natl Acad Sci USA. 105(36):13451–13455.
25. Walker MM, Diebel CE, Haugh CV, Pankhurst PM, Montgomery JC, Green CR. 1997. Structure and function of the vertebrate magnetic sense. Nature. 390(6658):371–376.